Master's Thesis

M.Sc. in Electronics Engineering

Analysis and modelling of RAFOS signal propagation under the Antarctic sea-ice for positioning Argo floats

Author: **Stefanie Spiesecke**

Supervisors: Prof. Dr.-Ing. Dieter Kraus

(Hochschule Bremen)

Dr. Olaf Boebel

(AWI)

Submitted:
February 2018

HSB
Hochschule Bremen
City University of Applied Sciences

ALFRED-WEGENER-INSTITUT
HELMHOLTZ-ZENTRUM FÜR POLAR-
UND MEERESFORSCHUNG

Erklärung über das eigenständige Erstellen der Arbeit

Hiermit versichere ich, dass ich die vorliegende Arbeit oder die von mir im Rahmen der Gruppenarbeit verantworteten, entsprechend gekennzeichneten Teile der Arbeit selbständig verfasst und keine anderen als die angegebenen Quellen und Hilfsmittel benutzt habe. Die Stellen der Arbeit, die anderen Werken dem Wortlaut oder dem Sinn nach entnommen wurden, sind durch Angaben der Herkunft kenntlich gemacht.

Diese Erklärung erstreckt sich auch auf in der Arbeit enthaltene Grafiken, Skizzen, bildliche Darstellungen sowie auf Quellen aus dem Internet.

Die Arbeit habe ich in gleicher oder ähnlicher Form auch auszugsweise noch nicht als Bestandteil einer Prüfungs- oder Studienleistung vorgelegt.

(Nur bei zusätzlicher elektronischer Abgabe: Ich versichere, dass die eingereichte elektronische Version der Arbeit vollständig mit der Druckversion übereinstimmt.)

Stefanie Spiesecke

Matrikelnummer 367263

Bremen, den 31.01.2018

_____

Stefanie Spiesecke

ABSTRACT

The Alfred-Wegener-Institute maintains a large-scale oceanographic observatory in the Southern Ocean, HAFOS (Hybrid Antarctic Float Observing System). Several deep sea moorings of this observatory host sound sources, allowing acoustic tracking of free floating under-ice profiling Argo floats. These floats contribute to the Argo project, which collects oceanographic data of the upper 2000m by over 3500 floats worldwide. As the Southern Ocean's seasonal ice coverage prohibits year round surfacing and satellite based position fixes, positioning during the float's under-ice periods is achieved using RAFOS signals, acoustical upsweeps from 259.38 Hz to 260.9 Hz, which can be detected by the float's RAFOS receiver. The float's position is determined by triangulation on basis of the distances, i.e. signal travel time, from the moored sound sources, which positions and sweep times are known. Distances are calculated from the travel time of the RAFOS signal.

Alongside the sound sources, HAFOS moorings host passive acoustic recorders. To investigate potential effects of environmental conditions, especially the ice coverage along the acoustic path, on the quality of received RAFOS signal, several such acoustic records were analyzed. Three sound source/recorder pairings in the Weddell Sea and four pairing located along the Greenwich Meridian were analyzed. Acoustic records were correlated with the known RAFOS reference signal to determine correlation heights as well as time-of-arrivals of RAFOS signals. Results reveal a correlation between sound pressure level decrease of the RAFOS signal and the formation of sea ice as well as a correlation of the received signal's sound pressure level and the correlation height. From the known source level of the sound sources and the received level in the recordings, transmission loss was calculated and compared to results from BELLHOP raytracing model runs to better understand the factors driving the observed variability. Model outputs suggest a high dependence of the received signal level on the relative depths of the sound source and receiver pairing. On the basis of the results from this thesis, mooring layouts for the sound sources might be improved in future deployments.

TABLE OF CONTENTS

1. MOTIVATION

The Alfred-Wegener-Institute (AWI) entertains long-term oceanographic observations to monitor marine climate change throughout the Weddell Sea, Antarctica. Since major parts of the Weddell Sea remain ice-covered during most of the year, however, oceanographic winter data are limited to positions occupied by long-term oceanographic moorings.

To improve the availability of wintertime data throughout the Weddell Sea, autonomous drifters, so-called floats, were and are deployed on a regular basis during the summer expeditions to collect oceanographic profiles once every 10 days while drifting with the currents for the ensuing months and years. Being integrated with the Argo project, which is part of the integrated global observation strategy, the floats record data on temperature, salinity and other physical or eventually biological parameters throughout their lifetime, lasting multiple years. An ice-detecting algorithm prevents the floats from surfacing while the ocean surface is ice-covered, protecting the float from damage (Klatt et al. 2007). Thus positioning by any satellite positioning system during winter is not feasible.

As described in Klatt et al. (2007), the Argo floats used by the AWI are capable of detecting so-called RAFOS signals, acoustic upsweeps from 259.38 Hz to 260.9 Hz, generated by each of several sound sources integrated to the oceanographic mooring array. The floats detect signals onboard by correlating the received acoustic data with the known initial signal and save the time of arrival and the correlation height of incoming RAFOS signals.

When resurfacing after winter, floats send all hitherto unsent data to the AWI via Iridium satellite communication. Time of arrival information provides the basis for positioning the float during the under-ice drifting period by triangulation.

This thesis aims at improving the understanding of the signal propagation and quality of the RAFOS sound signal in the Weddell Sea area. To better understand potential effects of environmental conditions on the propagation of the RAFOS signal, recorded signals from the acoustic recorders will be analyzed and correlated with environmental parameters. The analysis thereby focusses on the influence of ice coverage on the quality of received RAFOS signals. In addition, several ice-scenarios will be modelled with the BELLHOP model and results are compared to the measured data.

2. INTRODUCTION

A short introduction into the scientific background and the principles of underwater acoustics applying to this thesis will be given in the following chapter.

Figure 1 shows the region, which the data analysis is focused on. The Weddell Sea lies in the Atlantic part of the Southern Ocean. It is ice-covered during austral winter and in the southern parts also partially throughout the summer.
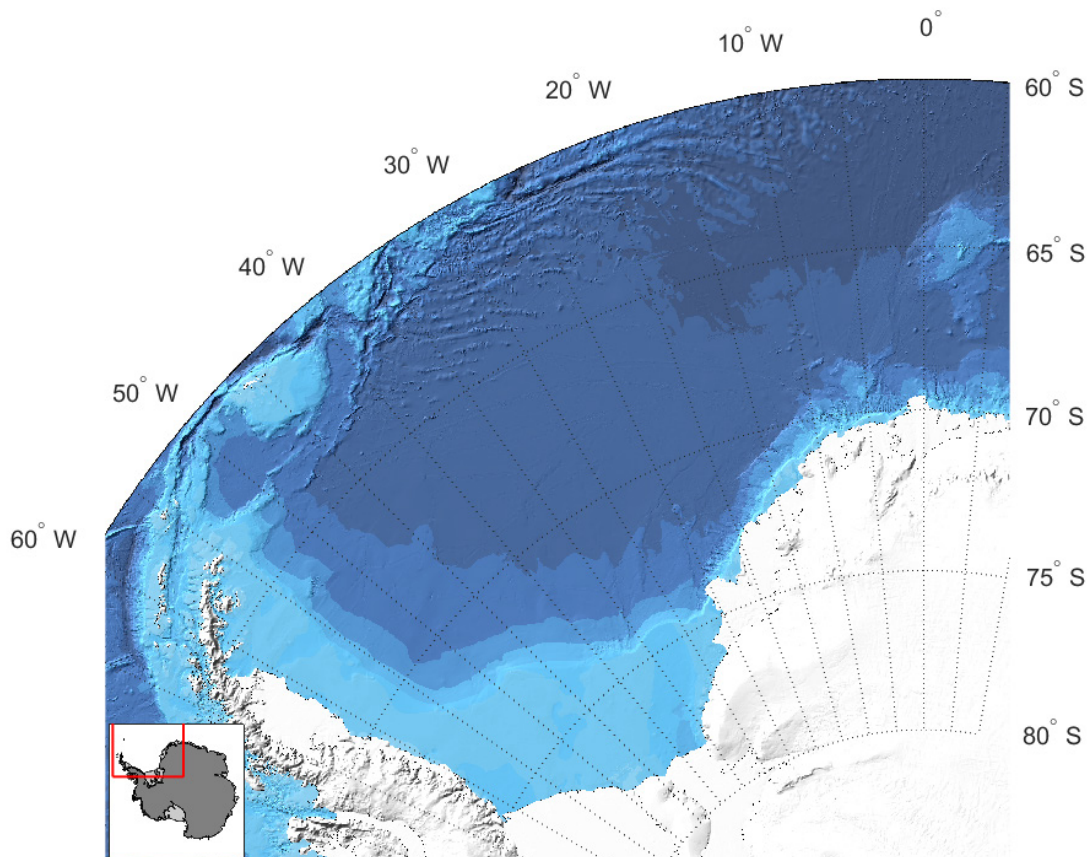

Figure 1: The region of interest: The Weddell Sea, Antarctica, which is the Atlantic part of the Southern Ocean.

2.1 SCIENTIFIC BACKGROUND

2.1.1 Physical Oceanography in the Southern Ocean

Processes in the Southern Ocean play an important role in the worlds' current and climate system. Numerous ocean-ice-atmosphere interactions and mixing processes around the Antarctic continent modify the water masses and induce horizontal and vertical exchange. The production and export of dense waters pose an important component of the global climate system. Water masses with higher density sink and form the so-called deep and bottom water masses. The resulting deep and bottom water masses are spread, forced by various physical

processes, the topography and atmospheric forcing conditions. The Weddell Sea current runs clockwise along the Weddell Sea continental slope and exits on various pathways at the tip of the Antarctic Peninsula, feeding the global current system. Thus, changes in the Weddell Sea current and water masses are of great interest for climate studies (Boebel 2013).

Because of the significant regional and temporal variability and the difficult accessibility of the region during the Antarctic winter, properties and volume of newly formed bottom water as well as impacts of long-term variations are scarcely explored. Therefore, data sets of sufficient spatial and temporal coverage are needed. The following sections describe efforts in the Weddell Sea to make advances in the investigation of the ocean interior on greater temporal and special scales.

2.1.1.1   The international Argo program

Argo is an international program to observe ocean temperature and salinity of the upper 2000 m on a global scale. It uses the data of autonomous drifters, called floats, that are able to profile the water column on a programmed schedule. Collected data is sent by satellite to base stations, validated and made openly accessible through the Argo data centers (ftp://ftp.ifremer.fr/ifremer/argo/ and ftp://usgodae.org/pub/outgoing/argo/ , both 2018). Figure 2 shows the current distribution of active Argo floats. As can be clearly seen from the map, floats are all but absent from high latitudes with regular sea ice cover.
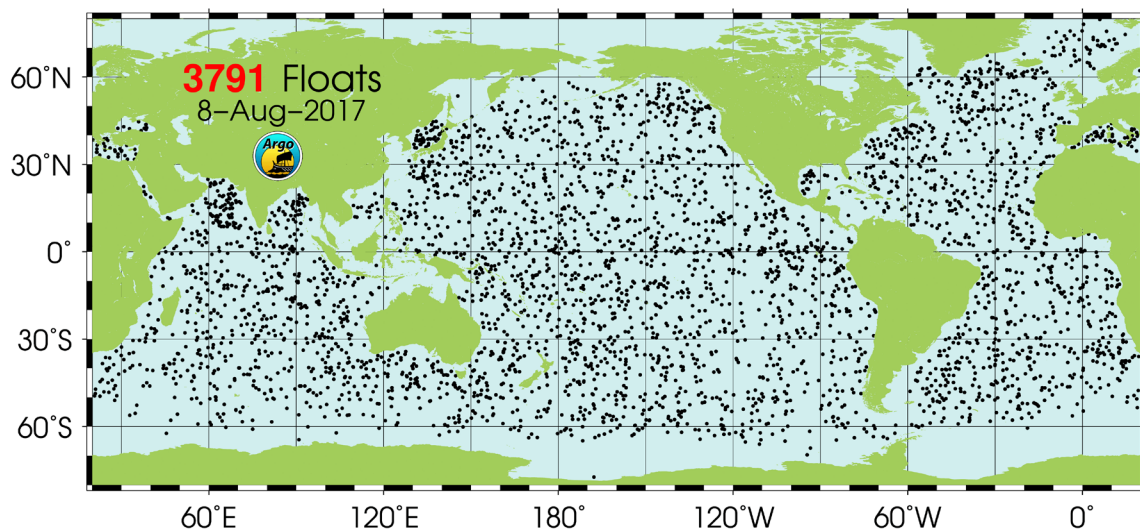

Figure 2: Distribution of active Argo floats on a global scale (downloaded from http://www.argo.ucsd.edu/ on August 8th, 2017)

2.1.1.2 HAFOS (Hybrid Antarctic Float Observing System) in the Southern Ocean

Data collected by moorings and from occasional wintertime expeditions provided so far the only hydrographic winter data for a long time. Sea ice poses a significant risk for autonomous platforms such as floats. By developing ice-resilient floats and deploying and an array of sound sources for under water tracking, the AWI contributes oceanographic data to the international Argo project from the Atlantic Sector of the Southern Ocean (Figure 1), including winter data. This effort forms an integral part of HAFOS, which comprises different platforms for the observation of water masses in the Arctic as well as the Antarctic with moorings located along the Greenwich meridian from 59° S towards the Antarctic Continent and throughout the Weddell Sea. Currently the array comprises 16 moorings, of which 9 host sound sources for the tracking of floats operating under-ice (please refer to the following sections for more detailed descriptions). The mooring array is refurbished every 2-3 years during scientific expeditions with the German research vessel 'Polarstern'. During these cruises, Argo floats are deployed throughout this part of the Southern Ocean. Alongside the sound sources and further oceanographic equipment, acoustic underwater recorders are fixed to the moorings. Originally used to explore the distribution and migration patterns of marine mammals, they also provide the basis for the analysis of the quality of signals originating from the sound sources.

2.1.1.3 Instrumentation

Sound Sources

The RAFOS system is an advancement of the tracking method of early floats described by Swallow in 1955. These early floats actively transmitted signals which were received and tracked by ship borne hydrophones (Swallow 1955) to investigate deep currents as suggested by Stommel (1955). The floats were drifting at depths of the SOFAR ('Sound Fixing And Ranging') channel (please refer to Chapter 2.2.2) to enable tracking over long distances, hence the name SOFAR float. The advent of satellite telemetry allowed switching source and receiver, as now data collected by the drifting float could be transmitted at the end of the mission. Analog to the switching of source and receiver, 'RAFOS' originates from the acronym inversion for 'SOFAR' (Rossby et al. 1986). It consists of moored sound sources, sending acoustic signals at a known time for positioning of autonomous underwater profilers (floats) or gliders. A linear acoustic upsweep from 259.375 Hz to 260.898 Hz over 80 s is send from modern RAFOS sound sources. Sound pressure level of the sources usually lies between 170 dB re 1µPa and 180 dB re 1µPa, depending on the type of source.

RAFOS sound sources generally consist of 2 main parts; a pressure housing containing electronics and power supply and the resonance tube, including the transducer. Depending on the type of the sound sources the electrical and mechanical set-up varies. Sound sources used

in the course of this thesis are of type NTSS manufactured by Develogic GmbH, Hamburg, Germany.

Floats

Modern Argo floats are expendable drifting sensor platforms deployed for long-term observations. They consist of a swim bladder, enabling to change the density of the float and thus being able to change operation depth. Operation of floats is completely autonomous. Drifting depth of the AWI floats is 800 m, while profiles are measured in the upper 2000 m. Floats used by the AWI in the Southern Ocean are mainly of the type NEMO (NAVIGATING EUROPEAN MARINE OBSERVER), which are equipped with an ice avoidance algorithm (Klatt et al. 2007). Because tracking using GPS or Iridium is not possible whilst a float stays submerged, they are equipped with a RAFOS-2 hydrophone. RAFOS-2 hydrophones (Teledyne Marine) have a sensitivity of -195 dB re 1V/µPa (@ 20°C). A time frame of 2 hours is set in which the RAFOS acoustic receiver is active, detecting signals from the sound sources deployed in the area.

The RAFOS acoustic receiver is a heterodyne receiver with a first intermediate frequency of 38.5 Hz. According to Rossby et al. (1986), this provides good image rejection and bandpass filtering. After a second mixer, it is sampled by the microprocessor at 10 Hz and hard limited, resulting in a discrete signal of 800 bit length, varying between Hi and Low. This process removes amplitude variations from the signal so only phase information is used in the correlation process. An XOR operation is performed on the digitized signal with a reference signal. (König and Zenk 1992). Maximum correlation is saved along with the time-of-arrival. After the float was able to resurface and send all saved data, correlation information is used to determine the position of the float during the subsurface drift period.

2.1.1.4 Acoustic tracking of floats

The acquired and stored information on time-of-arrival (*ToA*) and correlation heights of the RAFOS signal from the floats are displayed in form of the *ToA* versus date scatter plot, created by the tracking program ARTOA (Wooding et al. 2005). This scatter plot is used by the analyst to identify valid *ToA*s and assign these to specific sound sources as a first step in generating float trajectories. Thereby, drifts of both, the float's and sound source's clocks need to be accounted for. Correlation height as well as the coherence of time-of-arrivals (on the basis that a steady float movement can be assumed) are utilized as quality indicators for signal validation and assignment.

2.2 THE OCEAN AS AN ACOUSTIC WAVEGUIDE

Sound is a mechanical disturbance that travels through a fluid (Medwin and Clay 1997). This disturbance is generally described by incremental pressure (i.e. the difference between actual pressure and static pressure).

Several physical effects influence the propagation of acoustic pressure disturbances. Reflection occurs at obstacles and at boundaries like the sea surface and bottom. When experiencing changes in sound speed, refraction occurs. Pressures of independent sound waves will interfere constructively or destructively.

2.2.1 Mathematical description of sound propagation

Mathematically the propagation of acoustic waves is described by the wave equation. It describes the evolution of acoustic pressure as a function of space and time (Jensen et al. 2011).

The wave equation for pressure describing propagation of sound in three dimensions is:

$$\nabla^2 p - \frac{1}{c^2}\frac{\partial^2 p}{\partial t^2} = 0$$

$p =$ acoustic pressure, $c =$ sound speed, $t =$ time

When we assume our source being the center of a sphere in an infinite three dimensional medium, the solution to the wave equation has been determined to be:

$$p(r,t) = \frac{p_o}{r}e^{i\omega(t-\frac{r}{c})}$$

$r =$ radius of sphere, $\omega = 2\pi f =$ angular frequency, $f =$ frequency

The wave fronts equally propagate away from the point source forming a sphere around the source. When the sphere is big enough, it is possible to approximate the wave front as a plane, neglecting its curvature, by applying a simple solution to the wave equation. This plane wave equation applies to sinusoidal waves in a one dimensional space with constant sound speed, the plane wave equation:

$$p(x,t) = p_o e^{i\omega(t-\frac{x}{c})}$$

$x =$ spatial dimension

The plane wave equation describes that surfaces of constant phase are planes normal to the propagation direction.

All solutions to the acoustic wave equation, including more complex solutions than the ones described above, build the basis to models trying to predict sound propagation under water. Chapter 2.3 gives an overview on sound propagation models.

2.2.2   Sound speed

Sound propagation speed in seawater is related to static pressure, salinity and temperature. Mathematically sound speed (c) is expressed as an empirical function of three independent variables: temperature (T in °C), salinity (S in ppm), and depth (z in m). Medwin and Clay (1997) provide a simplified version of this empirical function, which is considered accurate enough for most applications:

$$c = 1449.2 + 4.6 * T - 0.055 * T^2 + 0.00029 * T^3 + (1.34 - 0.01 * T) * (S - 35) + 0.016 * z$$

Sound speed profiles (sound speed vs. depth) provide the basis for the prediction of sound propagation. Some sound speed profiles are typical for different geographical regions.

Changes in the sound speed profile (SSP) occur amongst others due to seasonal and diurnal changes. The near-surface area is the most variable. Due to thermal heating from the sun and mixing by wind, there can be a significant change in the sound speed in the upper parts of the water. Seasonal variability is generally greater than the diurnal effect.

In non-polar regions, with wind mixing the upper layer, a so-called *surface mixed layer* is formed, its depth depending on the wind conditions. Below this *mixed layer* the temperature decreases with depth, as does the sound speed. This *thermocline* ends with the sound speed minimum when the influence of increasing pressure exceeds the influence of temperature changes. The sound speed minimum is the axis of the deep sound channel (also SOFAR channel - SOund Fixing And Ranging). The sound is trapped inside the channel by diffraction towards its axis and no attenuation due to bottom and surface contacts is absent. Below the axis of the SOFAR channel the sound speed starts increasing, driven mainly by increasing pressure in the *deep isotheral layer*.

Ice coverage and heat loss on the surface area lead to a generally different sound speed profile in Polar Regions. The water is coldest at the surface and thus the sound speed is increasing with depth without a sound speed minimum in the water column. Figure 3 provides a general overview on an exemplary sound speed profile, including an example for a polar region sound speed profile (dashed line).
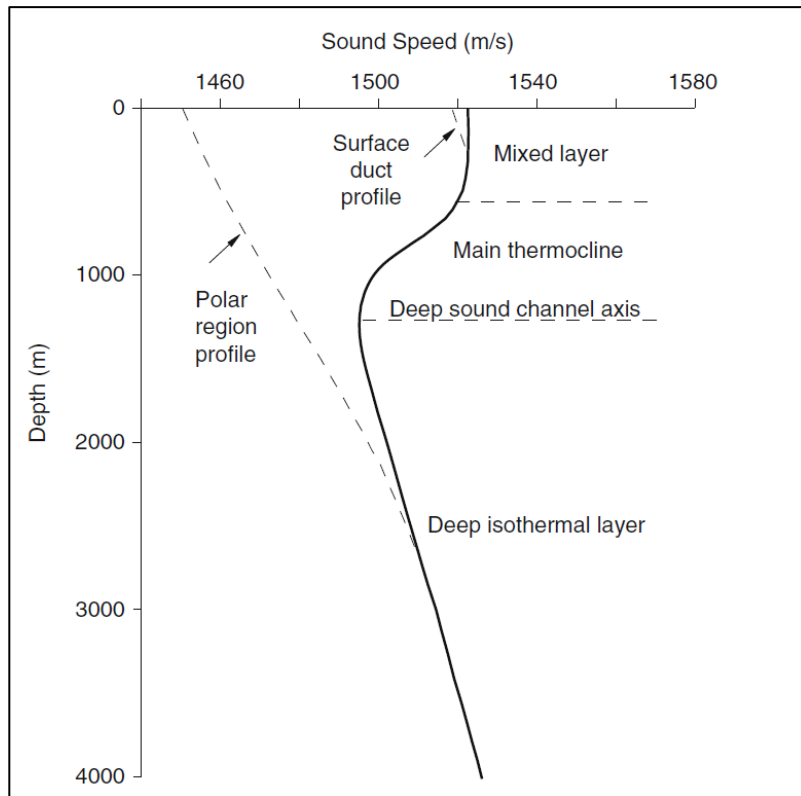
Figure 3: Sound speed profile general description (from Jensen et al. 2011)

2.2.1 Sonar equation for passive systems

The (one-way) passive sonar equation assumes separate transmitters and receivers of the acoustic signal. The source emits a signal with a source level *SL*, given in dB re 1μPa at one meter from the source. Signal intensity is reduced by spreading and absorption (transmission loss in dB re 1μPa, *TL*).

$$Received\ signal\ intensity\ (\text{dB re 1μPa})\ RL\ =\ SL - TL$$

2.2.2 Transmission Loss

Acoustical signal intensity weakens with range by geometrical spreading, attenuation in the water column, as well as the interaction with the upper and lower boundaries. Transmission loss is the relation between the nominal intensity (I_0) and the sound intensity at a distance *r* (I_r).

$$TL = 10 \log_{10} \left(\frac{I_0}{I_r} \right) \text{ in dB re 1μPa}$$

8

2.2.2.1 Geometrical spreading

Propagating sound is subject to transmission loss due to geometrical spreading. In an ocean environment, depending on the ratio of water depth to wavelength, geometrical spreading may be simplified as:

Spherical spreading

Acoustical power is radiated equally in all directions (three-dimensional) in a lossless medium without boundaries. This is considered to be the case where the radius of the sphere (*r*) is smaller or equal to the water depth (*d*). With power being defined as intensity by area:

$$P = 4\pi r_0^2 * I_0 = 4\pi r_r^2 * I_r \text{ , and } r_0 = 1 \text{ m}$$

$$TL_{sph} = 10\log_{10}\left(\frac{I_0}{I_r}\right) = 10\log_{10}(r^2)$$

$$TL_{sph} = 20 * \log_{10}(r) \text{ in dB}$$

Cylindrical spreading

In case the medium is limited by boundaries, in the ocean this being surface and bottom, and the distance to the point source is $r \gg d$, power is crossing a cylindrical surface of increasing radius *r* (in m), centered around the source, thus:

$$P = 2\pi r_0 h_0 * I_0 = 2\pi r_1 h_1 * I_r \text{ , and } r_0 = 1 \text{ m}$$

$$TL_{cyl} = 10\log_{10}\left(\frac{I_0}{I_r}\right) = 10\log_{10}(r)$$

$$TL_{cyl} = 10 * \log_{10}(r) \text{ in dB re } 1\mu\text{Pa}$$

In between there is a transition zone with a combination of both cases.

2.2.2.2 Sound attenuation

Part of the acoustic energy of propagating sound is continuously transformed into heat. Together with scattering on inhomogeneities, absorption leads to a decrease of sound intensity over distance. This is strongly depending on frequency, as different physical effects lead to the attenuation of sound at different frequencies.

- Water viscosity, increases with squared frequency
- Relaxation of magnesium sulphate (MgSO4) molecules, $f < 100$ kHz
- Relaxation of boric acid (B(OH)3) molecules, $f < 1$kHz

(Lurton 2002)

Several empirical formulae exist for the calculation of attenuation coefficients in sea water, varying in their complexity, relating the loss to frequency, pressure (depth), and salinity. The attenuation coefficient is given as α in dB km^{-1}. It decreases strongly with frequency and temperature, but also varies with depth and salinity.

As this thesis analyzes low frequency signals (259.38 Hz – 260.9 Hz) and attenuation thus will mainly be attributed to the relaxation of boric acid, a simpler formula developed by Thorp is sufficient to calculate the absorption coefficient. Thorp's formula is valid for frequencies from 100 Hz to about 3 kHz (Thorp 1967):

$$\alpha_T = \frac{0.11 f^2}{1 + f^2} + \frac{44 f^2}{4100 + f^2} \text{ in dB km}^{-1}, \quad \text{with } f \text{ in kHz}$$

2.2.2.3 Losses at the upper and lower acoustic boundaries in the ocean

Rough boundaries cause attenuation of the acoustic field in the ocean by scattering of the acoustic wave. The attenuation increases with increasing frequency. Scattering depends on the degree of roughness at the boundaries. With increasing roughness, scattering increases and the sound intensity in the specular direction is reduced. Furthermore, the backscattered part of the sound, the reverberation, contributes to the background noise and thus reduces the signal-to-noise ratio (*SNR*) of the signal of interest, which influences the performance of active systems.

Seabed

Seabed properties influence the amplitude of the reflected signal by transmission of part of the incident acoustic energy into the bottom. At low frequencies, sound potentially propagates through the sediment and back into the water. The loss depends on the sound speed in the bottom (which is affected by gradients and layering) and by roughness. While soft, muddy seabeds have a low reflection coefficient, hard, rocky bottom lead to almost complete reflection and very low losses of acoustic energy.

Sea surface

Sea surface properties can be subject to sudden changes. In case of an ice-free ocean surface wave conditions play a major role in the roughness of the sea surface and thus the reflective properties of the water – air boundary.

Air bubbles introduced into the water column, for instance, lead to reflections at their surfaces and thus a loss of energy in direction of interest. Furthermore, noise induced into the water by the motion of the waves will lower any signal-to-noise ratio.

Additionally to the wind induced effects, the seasonal ice coverage and its variation in thickness, roughness and ridging has a significant influence on sound propagation properties in polar regions. Alexander et al. (2013) state that there is a strong dependence on the type of ice coverage for transmission quality of signals. Two main parts influence the acoustic properties of sea ice:

- material properties: growth stage, ice as an acoustic medium
- mechanical properties: shape and size of ridging, ice as a boundary layer

The impact on acoustic properties of sea ice are strongly depending on the growth stage of forming sea ice. Jezek et al. (1990) separate three states: slush, growing and consolidated. Especially the differences in porosity, permeability and roughness attributed to the different stages have an effect on acoustic coupling into the ice, as well as the attenuation through the ice. Their study, however, was employed with high frequency signals at 188 kHz.

Yew and Weng (1987) modelled sea ice as a transversely isotropic brine-saturated porous medium. They noted that ice porosity has a noticeable effect on the wave reflectivity. The effect, however, becomes small with decreasing grazing angle of the incident wave and decreasing frequency. This backs up the results from experiments undertaken by Yang and Votaw (1981). Data from exploding light bulbs was recorded by an array of hydrophones, which were submerged beneath the sea ice along the experimental site. The experimental site consisted of ice flows with ice-depths, varying from 1.5 m to 4.9 m. According to their work, even smooth ice plates cannot be treated as totally reflective for frequencies between 200 Hz and 1 kHz and grazing angles between 14° and 26°. They assume that most of the reflection loss at smooth, flat ice could account for a significant part of the transmission loss in Arctic oceans, at least for this particular frequency range.

Additionally to the growth stages of ice, mechanical processes change the thickness and bottom roughness of the ice canopy, and thus may change the acoustic property as a boundary layer. Shearing and compression of ice floes within a closed ice cover leads to the breaking up of ice blocks at their sides and the pressing of those blocks under or on top of adjacent ice floes. Whole ice flows can also be pushed over each other, which is referred to as rafting (Marchenko and Makshtas 2005). These mechanical features undergo constant changes due to freezing and melting processes, as well as the compression and relaxation of the ice field induced by currents and wind. As sea ice hence is a greatly range and time varying surface layer, many studies on the propagation of acoustic waves under the sea ice use simulated ice conditions. One approach, used by Alexander et al. (2013) is the simulation of ice profiles based on measured or predicted sea ice statistics.

2.2.3 Ambient Noise

Underwater ambient sound is sound "that would be present in the absence of a specified activity" (ISO 2017). Ambient sound can be anthropogenic (e.g. shipping) or natural (e.g. wind, biota). The term ambient noise in this context will describe "sound except acoustic self-noise and except sound associated with a specified signal".

Ambient noise levels in the Southern Ocean are strongly affected by the annual variation of the sea-ice cover. In a study on different environmental contributors to the ambient sound in the Southern Ocean, Menze et al. (2017) describe the relation between increasing sea-ice concentration, area and thickness and decreasing sound levels and increases by contributions of distant sources. Depending on the frequency composition, ambient noise might mask the signal of interest, thus leading to reduced detection rates.

2.3 MODELLING SOUND PROPAGATION IN SEA WATER

Paul C. Etter broadly defines modeling as a method for organizing knowledge accumulated through observation or deduced from underlying principles (Etter 2003). Modelling is intended to generalize and abstract. Most underwater acoustic models treat the ocean as a deterministic system, which of course is only an approximation. This can lead to problems when comparing it to observational data, which are naturally non-deterministic for a natural system like the ocean.

Depending on the type of signal characteristics (frequency, modulation, duration) and the provided information on the environment, different model types exist. Figure 4 from Jensen et al. (2011) schematically shows five essential types of numerical sound propagation models employing different solutions to the full wave-equation (see Chapter 2.2.1).

Models, which permit ocean environments to vary with depth only, are called *range independent*. *Range dependent* models also permit horizontal variations in the environment (sound speed profiles and boundary conditions). While ray tracing, parabolic equation (PE), and direct finite-difference (FD) or finite element (FE) solutions are applied directly to range varying environments, fast field program (FFP) and normal mode (NM) lead to range independent solutions, but may be extended to find range dependent solutions.
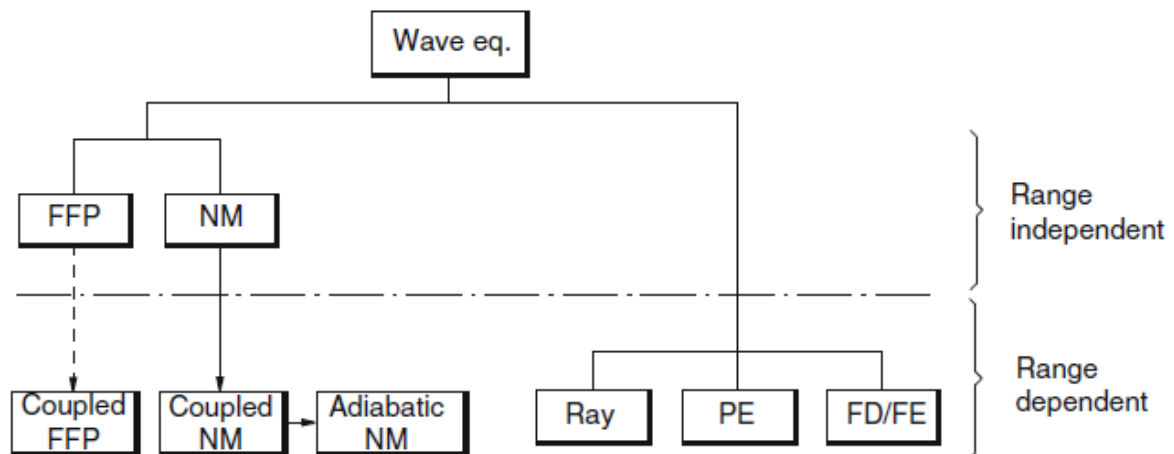
Figure 4: Overview on five essential models for underwater sound propagation from Jensen et al. (2011).

In geometrical acoustics the structure of an acoustic field is modelled as set of acoustical rays. The wave equation is solved numerically in this case. A ray is the normal vector of a wavefront, pointing in the direction of propagation. The simplest form of ray models trace rays by repeatedly applying the Snell-Descartes law. It relates the angles of incidence and refraction at a layer boundary (Figure 5). The sound thus turns toward regions of slow speed.

$$\frac{\sin \theta_1}{\sin \theta_2} = \frac{c_1}{c_2}$$
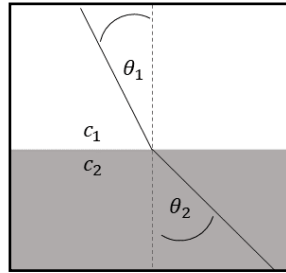
Figure 5: Drawing of snell's law: layer 1 with incident angle θ_1 and sound speed c_1 and layer 2 with θ_2 and sound speed c_2

In general, ray tracing is used for models with high frequencies of order kilohertz or above. However, even in lower frequency ranges ray theory models might hold some advantages towards other models with better accuracy when computational speed is a critical factor and environmental uncertainty poses severe constraints on the attainable accuracy (Jensen et al. 2011). An important rule that Jensen quotes for the applicability of ray models, is that the acoustic wavelength should be substantially smaller than any physical scale in the problem. So in effect, this means the wavelength (λ) should be small compared to the water depth (d), bathymetric features and internal features like surface ducts. Smoothing out such features can often improve the ray tracing result. Most ray tracing models include further aspects of wave propagation to account for intensity losses along the rays. These are mainly losses attributed to geometrical spreading (refer to Chapter 2.2.2.1), attenuation (refer to Chapter 2.2.2.2) and interactions with boundaries (refer to Chapter 2.2.2.3). Additionally they may include calculations on the resulting field at a receiver, modeled by summing the contributions of the various rays, with appropriate amplitudes and delays (Lurton 2002).

3. METHODS

3.1 DATA AVAILABILITY AND PREPROCESSING

Data and metadata originated from acoustic recorders and CTD loggers moored alongside RAFOS sound sources in oceanographic moorings, from CTD casts carried out during RV Polarstern expeditions, from a profiling Argo float and from online sources. Table 1 gives account of the origin of the data used. Analysis was conducted using various MATLAB® toolboxes, custom developed functions and scripts.

Parameter	Platform: Instrumenttype	Origin	Time	Resolution (if applicable)
Temperature	Mooring: SM37	AWI	2012/2013; 2014-2016	stationary, every 120 min
Salinity				
Pressure				
Temperature	Ship: SBE911plus	AWI	2012/2013; 2014-2016	~1 m vertical, one profile at every station, complete water column
Salinity				
Pressure				
Temperature	NEMO Float 272	AWI	2017	Upper 2000m, one profile every10 days
Salinity				
Pressure				
Bathymetry	various	Bedmap2	--	--
Thin sea ice thickness	Satellite: SMOS sensor	seaiceportal*	2012/2013 2014-2016	12.5 km x 12.5 km horizontal grid
Sea Ice concentration	Satellite: AMSR2 sensor	seaiceportal*	2013; 2015/2016	6.25 km x 6.25 km horizontal grid
Acoustic data	Mooring: SonoVault	AWI**	2012/2013; 2014-2016	f_s=5.3 kHz or 6.8 kHz ,24 bit, continuous

Table 1: Origin of analyzed data; *) www.seaiceportal.de (Grosfeld et al. 2016); **)Alfred Wegener institute, Helmholtz center for polar and marine research.

3.1.1 Analyzed propagation paths

Six sound source / acoustic recorder pairings deployed in 2012/2013 were selected for analysis on behalf of data availability from recorders, position in the southern ocean and distance between moorings. Record durations ranged from 231 to 296 days. An additional pairing with recordings ranging from Dec2014 to May2016 was included in the analysis as it comprises two freezing and one melting period.

Each pairing is labelled with an individual ID. Table 2 summarizes information on the analyzed paths and associates them with the respective path ID. The Weddell Sea IDs use 'WS' for Weddell Sea and the direction 'W' for westward and 'E' for eastward as well as '1' and '2' for two different recorders in the receiving mooring. Greenwich Meridian IDs use 'GM' for Greenwich Meridian, 'S' for the southern part, 'N' for the northern part and 'T' for the complete

(total) path from South to North. The year given after 'GMT' helps to identify the mooring period. Instruments of path 'GMT 2013' were moored from Dec. 2012 to Dec. 2014, while instruments of 'GMT 2015' were moored from Dec 2014 to Dec 2016.

Path ID	Mooring: Source	Sound Source ID	Depth [m]	Mooring: Receiver	Recorder ID	Depth [m]	Recording duration [days]	Distance [km]
WSW	AWI209	D0025	805	AWI208	SV1030	956	291	432.5
WSE1	AWI208	D0029	856	AWI209	SV1028	1007	283	432.5
WSE2	AWI208	D0029	856	AWI209	SV1029	2516	295	432.5
GMS	AWI231	D0024	830	AWI230	SV1009	949	286	53.4
GMN	AWI229	D0026	807	AWI230	SV1009	949	286	226.8
GMT 2013	AWI231	D0024	830	AWI229	SV1010	969	231	280.1
GMT 2015	AWI231	D0024	798	AWI229	SV1057	970	520	284.9

Table 2: Analyzed sound source/acoustic recorder pairings with associated IDs and path information. WS stands for 'Weddell Sea' and refers to the moorings which lie within the Weddell Sea basin. GM stands for 'Greenwich Meridian' and refers to moorings along the Greenwich Meridian. The map in Figure 6 shows all relevant mooring positions.
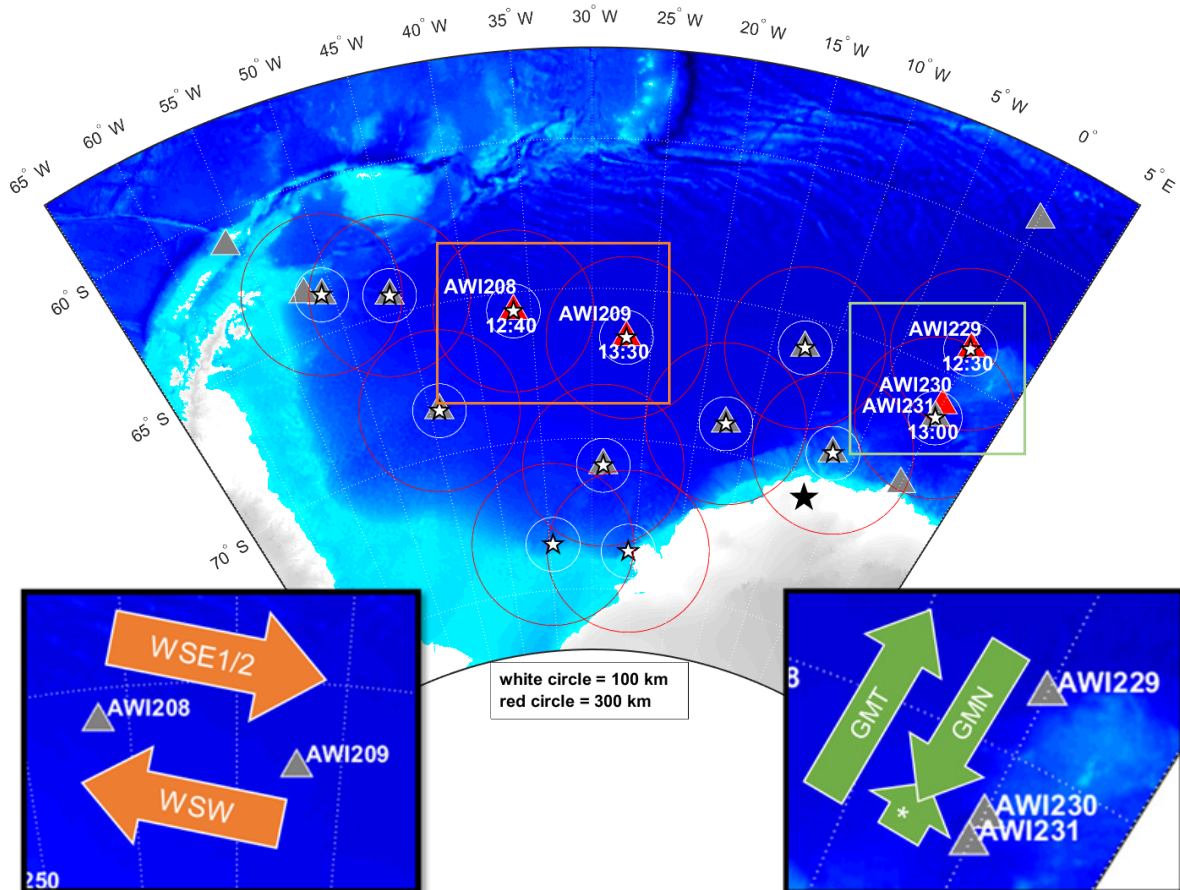
Figure 6: Map of the HAFOS array with sound source locations (white stars) and recorder positions (grey and red triangles). Red triangles mark recorders used in this thesis. Mooring positions relevant to this thesis are labelled with mooring IDs and sound source pong times. The circles around sound source positions mark different radii from the source (white: 100 km; red: 300 km). Bottom: close-ups on mooring positions with path IDs. The asterix (*) stand for path GMS.

A seamount, Maud Rise, is located east of the Greenwich Meridian moorings AWI230 and AWI231. Therefore, bathymetry is varying from about 3500 m water depth to over 5000 m water depth between AWI 231 and AWI229. Bathymetry along the Weddell Sea paths, in contrast, is rather smooth at water depths of 4700 m to 4800 m.

3.1.2   Sound Pressure Levels of RAFOS sound sources

For calculations of transmission loss along the propagation paths, source levels of the sound sources were included. Sound pressure levels of the analyzed RAFOS sound sources were measured during Polarstern expedition ANT-XXIX/2 on RV (Boebel 2013).

Resulting sound pressure levels of the analyzed sound sources were as follows:

Sound Source ID	Mooring ID	Date of measurement	Frequency at A_{max} [Hz]	Source Level A_{max} [dB re 1µPa]
D0024	AWI231	13.12.2012	260.6	174
D0026	AWI229	13.12.2012	259.6	174
D0025	AWI209	30.12.2012	260.3	172
D0029	AWI208	02.01.2013	259.2	171

Table 3: Measured sound pressure levels for the sound sources used in this study. A_{max} is the maximum amplitude within the RAFOS signal.

3.1.3   Acoustic recordings from acoustic recorders

Recorders relevant to this thesis were deployed in December 2012 during RV Polarstern expedition ANT-XXIX/2 (Boebel 2013) as well as in December 2014 during RV Polarstern expedition PS89. Recorders were of type SonoVault (Develogic GmbH, Hamburg, Germany). They were set to record continuously with sampling frequencies (f_s) of 5.3 kHz (2012/2013) and 6.8 kHz (2014/2015) at 24 bit, using a gain of 24 dB or 48 dB to files of 600 seconds lengths. Recorder gain was calibrated post recovery with a Brüel & Kjaer pistonphone calibrator. Built-in hydrophones of the type TC4037-3 have a sensitivity of -193 dB re 1V/µPa.

For the ensuing analysis, only data from recorders with valid post-deployment calibrations from deployments in December 2012 / January 2013 and one recorder from a deployment in December 2014 were included.

3.1.4   Physical oceanographic data

For input to the BELLHOP raytracing model, sound speed profiles were calculated. CTD recorders from different platforms provided temperature, salinity and pressure records to calculate sound speed profiles. Moored autonomous CTD recorders (SM37, Sea-Bird Scientific) delivered coarser vertical profiles, but year-round data at the mooring positions. They measured temperature, salinity and pressure every 120 minutes.

Ship-based CTD (SBE911plus, Sea-Bird Scientific) measurements, undertaken between deployments of moorings on expeditions ANT-XXIX/2 and PS89, were taken to create sound speed profiles with finer vertical resolution for the whole water column. These, however, were limited to a one-time measurement on each position during the expedition.

Float 272 delivered data for the upper 2000m in the inner Weddell Sea. Winter and summer profiles from this float are presented in Chapter 4.1.

For the investigation of variations in the deployment depth of sound sources and acoustic recorders, depth data from CTD measurements within the sound source moorings were analyzed.

3.1.5 *Bathymetry data and seabed properties*

Bathymetry profiles between two mooring positions were generated using MATLAB® functions from the Antarctic Mapping Toolbox, developed by Chad Greene (Greene et al. 2017). Data basis was the Bedmap2 data set (Fretwell et al. 2013).The data set includes a compilation of bedrock topography data from around the Antarctic continent.

The MATLAB® script *Bathy_along_path.m* extracts Bedmap2 bathymetric data. It projects the 2D grid data on the 1D path between the moorings. Depth values are averaged along the path, plotted and saved in a *.bty file format for the model input (Figure 7).
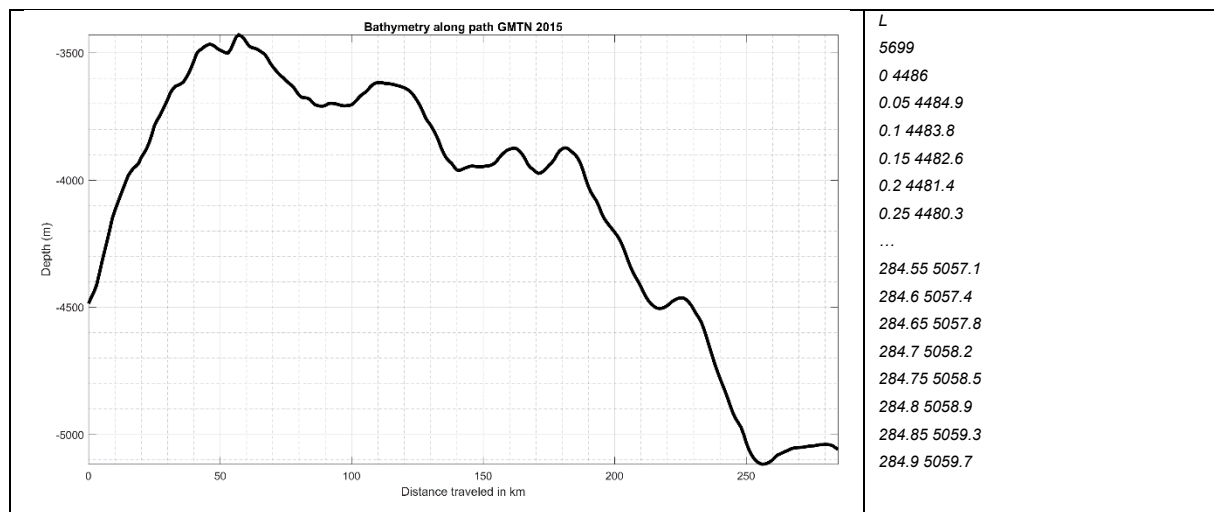
*Figure 7: Example for Bathymetry along Greenwich Meridian path GMT 2015 (left) and resulting *.bty file for model input. Note that the upper ordinate limit is not set to 0 (i.e. sea surface).*

For the model input seabed information from a study by Breitzke and Bohlen (2010) was applied. They summarized information from different papers regarding seabed properties in the Weddell Sea area (Table 4, next page). According to different sources (e.g. Kuhn and Weber (1993); Melles and Kuhn (1993);Michels et al. (2002)) the seabed in the area of interest is mainly covered by soft sediment.

V_P (m s^{-1})	V_S (m s^{-1})	ρ (kg m^{-3})	Q_P	Q_S	R	α_{crit} (°)	$x_{crit,3000}/2$ (m)	$x_{crit,400}/2$ (m)
1510	110	1250	1.5×10^6	1.5×10^6	0.1	83.4	25 938	3458
1600	330	1450	1.5×10^6	1.5×10^6	0.2	69.6	8082	1078
1670	400	1710	1.5×10^6	1.5×10^6	0.3	63.9	6130	817
1870	510	1930	1.5×10^6	1.5×10^6	0.4	53.3	4030	537

Notes: The normal incidence reflection coefficient R at the seafloor and the critical angle are computed for a P-wave velocity of 1500 m s^{-1} and a density of 1025 kg m^{-3} of sea water. The half critical distances are computed from the critical angles for 3000 m ($x_{crit,3000}/2$) and 400 m ($x_{crit,400}/2$) water depth. V_P is the P-wave velocity, V_S is the S-wave velocity, ρ is the wet bulk density, Q_P is P-wave quality factor, Q_S is S-wave quality factor, R is the normal incidence reflection coefficient at the seafloor, α_{crit} is the critical angle at the seafloor, $x_{crit,3000}$ is the critical distance for 3000 m water depth, $x_{crit,400}$ is the critical distance for 400 m water depth.

Table 4: Seafloor properties for the Weddell Sea from Breitzke and Bohlen (2010).

For the model input in this thesis, the following sea bed properties from Table 4 were selected:

- compressional speed 1600 m s^{-1};
- shear speed 330 m s^{-1};
- density 1450 kg m^{-3}; (1.45 g cm^{-3})
- attenuation is neglected

3.1.6 Sea ice data

Long-term data from the Southern Ocean regarding sea ice properties (e.g. sea ice thickness, ridging, snow coverage) is scarce. Most studies include ship-based visual observations and point measurements along ship tracks, mostly restricted to the Antarctic summer months. Sea ice thickness and snow coverage satellite measurements are currently under development.

Available long-term satellite products are year-round sea ice concentration data as well as the recent data on *thin sea ice thickness*, which is only available from April to October. Sea ice data were downloaded online from the University of Bremen homepage (https://seaice.uni-bremen.de/data/, downloaded July, 2017). The PHAROS (PHysical Analysis of RemOte Sensing images) group at the Institute of Environmental Physics (IUP, University of Bremen, Germany) calculates sea ice concentration charts on a daily basis. Data is provided in .hdf format, representing daily average values on a polar sterographic grid (6.25 km), readily extractable using the hdfread.m command in MATLAB®. Grid information is also available on the same platform. The source for this data is the Advanced Microwave Scanning Radiometer 2 (AMSR2) sensor data from the satellite "Shizuku" (GCOM-W1), which was developed by the Japan Aerospace Exploration Agency JAXA). The sensor is the successor of AMSR-E sensor, which was operating from 2003 - Oct2011 (Spreen et al. 2008).

For additional sea ice information, SMOS („Soil Moisture and Ocean Salinity") satellite data from the IUP Bremen was downloaded to get information on sea ice thickness. The Microwave Imaging Radiometer with Aperture Synthesis (MIRAS) creates images of radiation emitted in the microwave L-band (1.4 GHz). Originally, it was used for the measurement of soil moisture and ocean salinity as part of the ESA Living Planet Program. SMOS sea ice thickness data

analysis was developed by the IUP in Bremen (Huntemann et al. 2014) and shows young, sea ice coverage for up to 50 cm thickness. Because of the limited thickness, it will be referred to as '*thin sea ice thickness*' in this thesis. In the Antarctic, data cover a time span from 1 April until 30 of September. According to the authors, the procedure does not yield meaningful results during the melting season.

The MATLAB[®] script *Ice_along_path_amsr2.m* extracts AMSR2 data between two mooring positions, while *Ice_along_path_smos.m* provides likewise data from SMOS. *Thin sea ice thickness* on the path between two moorings was calculated and saved in an altimetry (*.ati) file on a daily basis. These files were generated as to function as surface input for the BELLHOP model.

Approximated acoustic properties for an air backed ice layer from Jensen et al. (2011), with the ice cover assumed to be a homogeneous and isotropic elastic plate with the following properties were included in the BELLHOP model run:

- Compressional speed 3500 m s^{-1}
- shear speed 1800 m s^{-1}
- density 900 kg m^{-3}; (0.9 g cm^{-3})
- compressional attenuation 0.5 dB λ_p^{-1}
- and shear attenuation 1.0 dB λ_s^{-1}

3.2 EVALUATION OF RAFOS SIGNALS IN ACOUSTIC RECORDINGS

Figure 8 illustrates the analytic steps taken, the names of the main programming scripts and their outputs.

Received RAFOS signals were extracted from the acoustic recordings to Waveform Audio File Format (in short: WAVE or WAV, file ending *.wav) files of 300 s duration ('snippets'). Within these, RAFOS signals were detected by correlation, providing time-of-arrival, signal level, noise level, SNR and various statistical values saved to a MATLAB® data file (file ending *.mat). The grey part of Figure 8 gives a simple overview on this part of the analysis.

Metadata was preprocessed for analysis in context with the RAFOS signals and for input to the BELLHOP model. Sea ice (Figure 8: blue), bathymetry (Figure 8: yellow) and sound speed (Figure 8: green) data from the area of interest is converted to formats suitable for the model input (please refer to Chapters 3.1.4, 3.1.5 and 3.1.6) or further processing, and plotted.

The so-called "environmental file" was generated for input in the BELLHOP model. The existing model functions were exectuted to generate Eigenray, impulse response and transmission loss calculations and plots (Figure 8: orange). For detailed description of the BELLHOP model refer to Chapter 3.3.1.

As programming platform served MATLAB® (Version R2017a), including the Signal Processing™ and Mapping™ toolboxes. Several functions from openly available MATLAB® toolboxes and from the MathWorks® file exchange are embedded into the scripts. Functions used in the scripts are listed in Table A.3 in the appendix.

Figure 8: Data flow of RAFOS signal analysis and modelling. Left: Signal analysis, upper right: Processing of environmental data, lower right: BELLHOP modelling

3.2.1 Generation of waveform files with RAFOS signal (snippets)

The MATLAB® script *RFSsnippets.m* was programmed in order to extract from the raw audio files the part within which the acoustic recordings of RAFOS signals were to be expected. To calculate of the position of RAFOS signals within the audio files, the following steps were taken:

The recorder clock is set to coordinated universal time (UTC), while sound sources are set to GPS. In 2013, the number of leap seconds between UTC and GPS was 16 s, which needed to be accounted for in the time calculations (2012-2014: UTC = GPS -16 s). The time of expected signal reception by the recorder (expected time-of-arrival, ToA_e) at the beginning of the deployment period was calculated. For the calculation the travel time (t_{tt}) between recorder and sound source, the time offset of the sound source from GPS time at mission start (t_{offset}), as well as the leap seconds between UTC and GPS (t_l) were added to the nominal sweep time of the sound source (st_n).

$$ToA_e \; (UTC) \; = \; st_n \; (GPS) \; + \; t_{tt} \; + \; t_{offset} \; + \; t_l$$

A buffer of 110 s before and after the expected sweep were added to the snippet length to account for any inaccuracies regarding the recorder's and sound source's time drifts, resulting in 300 s snippet length.

To include the clock drift of the recorder and the sound source, the relative total daily clock drift in seconds between recorder and sound source was calculated by subtracting the sound sources' daily drift from the recorders' daily drift and multiplying it by the number of days between the mission start and the current file.

RAFOS start time was corrected using the calculated drifts described above. Based on this calculation the acoustic file covering the calculated signal arrival time was opened and the calculated snippet period was saved to new waveform file. In case the snippet period was distributed over two consecutive files, both parts were extracted, merged and saved. This latter situation may have resulted in some missing samples within the signal.

3.2.2 Correlation of RAFOS signal in snippets

Correlation script *RFScorrelator.m* detects RAFOS signals by cross-correlating audio snippets with a noise-free reference version of the signal. For correlation the function *xcorr.m* was used. The reference RAFOS signal was created using the *chirp.m* function implemented in MATLAB®. For better comparison of the analyzed paths, correlation height (*ch*) was normalized to the maximum correlation height (ch_{max}) achieved throughout the deployment period of the corresponding propagation path. The resulting correlation coefficient (*cc*) is scaled to 0 to 100.

$$cc \; [\%] = \frac{ch}{ch_{max}} * 100$$

ToA is calculated using the lag between signal and reference signal at the maximum of the correlation coefficient (cc_{max}).

3.2.3   Improving number of false positive detections

Even if no RAFOS signal is present (i.e. masked by noise) in the data, the correlator would still provide a correlation maximum. In this case the correlation maximum can be situated at any position in the file, delivering a random time-of-arrival.

In a true RAFOS application with drifting RAFOS receivers the steadiness of motion (i.e. *ToA* at day x+1 is expected to be plausibly close to *ToA* at day x) can safely be used as guidance to further (in addition to correlation heights) discriminate between valid and invalid *TOA*s. Here, with moored sources and receivers, the expected *ToA* is – with the exemption of small fluctuations due to clock drifts and changes in sound speed – constant. Hence the the accuracy of the time-of-arrival may serve as additional indicator for the systems performance. After the correlation, a fitting line is calculated for the *ToA* scatter plot of valid *ToA*s. The relative distance to the line of every *ToA* data point was calculated. In the results section the absolute distance of the calculated *ToA* to the fitting line is referred to as relative *ToA* (*rel ToA*). All *ToA*s with a *rel ToA* distance of more than 5 s were regarded as false positives and set to NaN. NaN, the acronym for 'Not a Number', is used in programming to represent unrepresentable values.

3.2.4   Calculation of received levels and signal-to-noise ratio (SNR)

Additionally to correlation height and *ToA*, sound pressure level (*SPL*) of the received signal (received level = *RL*), SPL of noise (noise level = *NL*) and signal-to-noise ratio (*SNR*) were calculated and saved.

Sound pressure level (SPL) calculations

A 2nd order Butterworth bandpass filter from 259.3 Hz to 260.95 Hz and stopband attenuation of -60 dB was applied to the 80 s of the file containing the RAFOS sweep. Mean, median, maximum and standard deviation of the rms (root-mean-square) *SPL* in dB re 1µPa in the bandpassed signal were calculated and stored. The same calculations were performed on bandpassed samples of the snippet before and after the sweep, to calculate noise levels from the same band as the RAFOS signal.

SPL of *RL* and *NL* was calculated based on:

$$p = dc * \frac{1}{m} * \frac{1}{s} * \frac{1}{g}$$

with

$$m = \frac{dc_{FS}}{ADC_{in}}$$

$$ADCin = \text{Input range of analog} - \text{to} - \text{digital converter (ADC)}$$

$$= \pm 2.5 \text{ V at fullscale (FS) for SonoVault recorders}$$

$$dc = \text{digital counts (digital value in file)}, \quad dc_{FS} = 1e23 \ = \ 127.4 \text{ dB re 1μPa}$$

hence

$$p = c * \frac{ADC_{in}}{c_{FS}} * \frac{1}{s} * \frac{1}{g} = \frac{c}{c_{FS}} * ADC_{in} * \frac{1}{s} * \frac{1}{g}$$

$$\frac{c}{c_{FS}} = \text{normalized value from . WAV file } (0 - 1 \text{ zero to peak}) = x$$

hence

$$p = x * ADCin * \frac{1}{s} * \frac{1}{g}$$

And in logarithmic terms

$$SPL \text{ [dB]} = 20 * \log_{10}(x * ADCin) - SH - G$$

With

$$SH = \text{Hydrophone Sensitivity in dB re 1V μPa}^{-1}$$

$$G = \text{calibrated gain of acoustic recorder in dB}$$

Signal-to-noise ratio (SNR)

SNR was calculated using:

$$SNR \text{ [dB]} = RL - NL$$

$$RL = \text{ Received level signal}, \qquad NL = \text{Noise level}$$

Transmission loss (TL)

Transmission loss was calculated as:

$$TL \text{ [dB]} = SL - RL$$

$$SL = \text{ Source level of sound source}$$

3.3 MODELLING

3.3.1 Acoustic propagation modelling with the BELLHOP raytracing model

BELLHOP is a beam tracing model for predicting acoustic pressure fields in ocean environments. It was written in Fortran by Michael Porter as part of the Acoustic Toolbox (Porter 2011). Sound speed profiles, as well as top and bottom boundary (sea surface and bathymetry) parameters can be included in the calculation. It performs two-dimensional acoustic ray tracing within these limits. Several types of beams are implemented including Gaussian and hat-shaped beams, with both geometric and physics-based spreading laws. A variety of outputs including ray coordinates, transmission loss, amplitudes, and received time-series can be generated using the BELLHOP model (Rodriguez 2008).

This ray tracing model solves the dynamic ray equations to calculate amplitudes and acoustic pressure (Jensen et al. 2011). The ray equation for a system with cylindrical symmetry can be written as:

$$\frac{dr}{ds} = c\xi(s), \qquad \frac{d\xi}{ds} = -\frac{1}{c^2}\frac{\partial c}{\partial r},$$

$$\frac{dz}{ds} = c\zeta(s), \qquad \frac{d\zeta}{ds} = -\frac{1}{c^2}\frac{\partial c}{\partial z}$$

with

$$r(s) \text{ and } z(s) = \text{ray coordinates in cylindrical coordinates}$$

$$s = \text{arclength along the ray}$$

$$c(s)[\xi(s), \zeta(s)] = \text{tangent vector along ray}$$

Initial conditions:

$$r(0) = r_s, \qquad z(0) = z_s, \qquad \xi(0) = \frac{\cos\theta_s}{c_s}, \qquad \zeta(0) = \frac{\sin\theta_s}{c_s},$$

$$\theta = \text{lauching angle}, (r_s, z_s) = \text{sources position}, c_s = \text{sound speed at source position}$$

To obtain the ray travel time it uses:

$$\tau = \int_\Gamma \frac{ds}{c(s)}, \text{parameterized } [r(s), z(s)]$$

According to the ActUp (Acoustic Toolbox User interface and Post processor) manual (Bennett 2009), which includes the BELLHOP code, BELLHOP has a useful frequency range which extends lower than standard ray trace programs. Bennett (2009) advises to use it with extreme

caution in situations where the water depth or the size of any significant feature in the sound speed profile is less than 20 wavelengths as it inherently is a high frequency code. With water depths between 3500 m and 5000 m and a wavelength of 5.7 m these requirements for using BELLHOP are met.

$$\lambda = \frac{c}{f} = \frac{1480 \ \frac{m}{s}}{260 \ \text{Hz}} = 5.7 \ \text{m}$$

$$20 * 5.7 \ \text{m} = 114 \ \text{m}$$

3.3.2 General structure

The BELLHOP algorithm developed by Porter (2011), is also implemented in MATLAB®. Input parameters and options for the calculation of propagation paths are summarized in an environmental input file (*.env, see exemplary environmental file in Table A.2 in the Appendix section). Further input parameters, like bathymetry and surface structure, are provided in *.bty and *.ati files, respectively (See Chapter 3.1.5). The following figure (Figure 9) depicts the various input, output and plotting options implemented in the BELLHOP program.
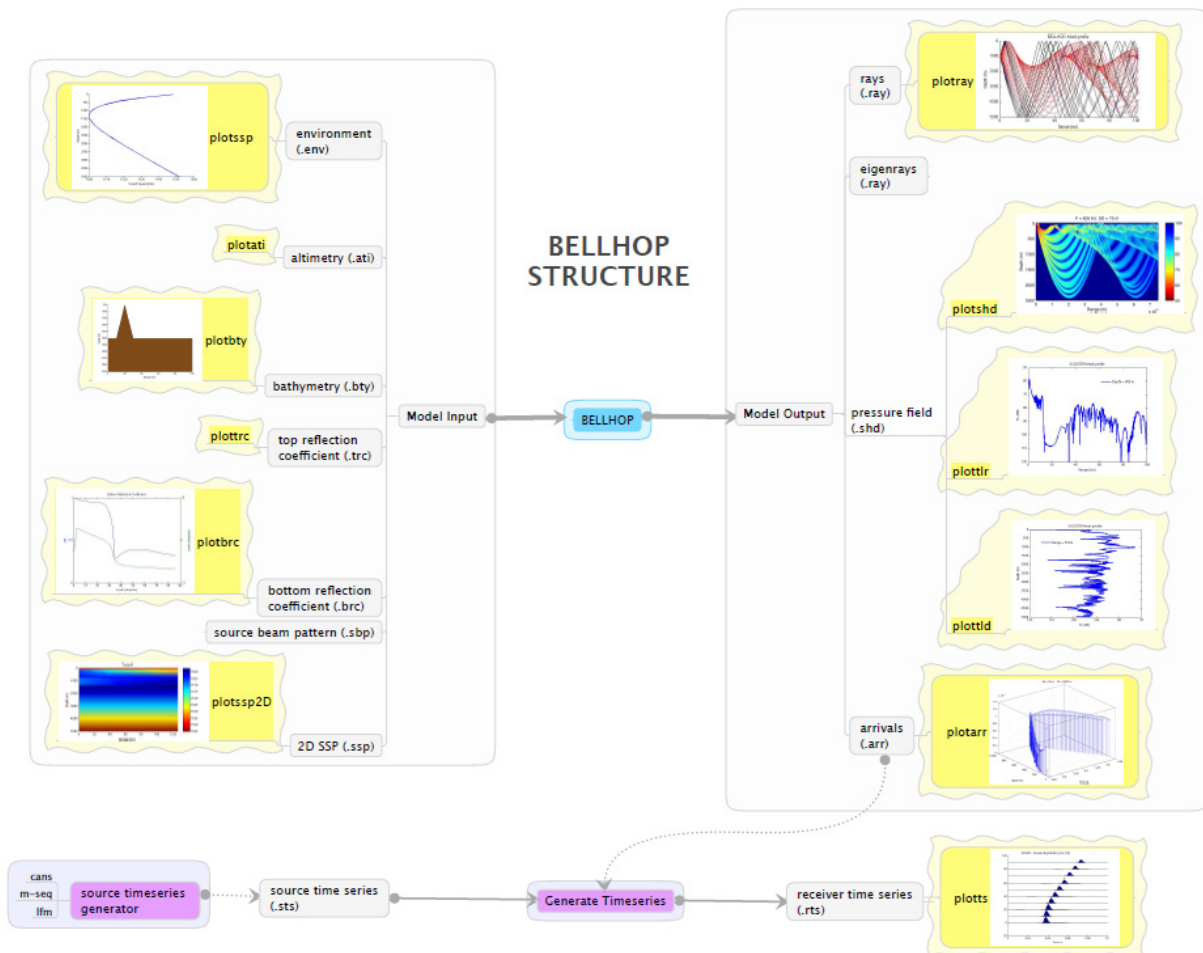
Figure 9: BELLHOP general structure (from Porter (2011)).

Sound speed profiles at the sound source position with a vertical resolution of about 100 m were used for the model input. Angles between -35 to 35 degrees were selected as the sound source features a preferentially horizontal emission pattern (private communication, Develogic Subsea systems GmbH, Hamburg, Germany).

The decision on the size of increments between those angles was left to the program, by setting the step size in the last line to '0'. Only for coherent transmission loss calculation on analyzed paths in the Weddell Sea it was set to a step size of approx. 2°, as otherwise computation time would have been disproportionately high.

Bathymetry data files, as described in Chapter 3.1.5, and thin ice thickness data files, as described in Chapter 3.1.6, were added to the model.

All sound source/recorder pairings were simulated including bathymetry, both without and with ice cover. Surface parameters applied include:

1. ice-free
2. ice coverage with *.ati files from 1st of May and 1st of June with the following parameter settings:
    - Compressional speed 3500 m s^{-1};
    - shear speed 1800 m s^{-1};
    - density 890 kg/m3; (0.89 g cm^{-3})
    - compressional attenuation 0.4 dB λ_p^{-1};
    - and shear attenuation 1.0 dB λ_s^{-1}

The following chapters describe the run types used for this thesis.

3.3.2.1   Raytracing / Eigenrays

The output file has the extension *.ray, containing the coordinates of each ray. Plots of the rays were created by **plotray('<filename.ray>')** function.

Eigenrays can be calculated using the same calculation as in the raytracing option, but by only saving the rays reaching the receiver from the source in the *.ray output file. The same plotting function applies for this calculation. In this thesis, only the Eigenray option is used.

3.3.2.1   Impulse response

To obtain the impulse response (arrival information) of the Eigenrays, BELLHOP provides array files which contain amplitude, phase information and travel time of each ray. It also saves take-off angle and number of bottom and surface bounces. Impulse response are displayed using **plotarr('<filename.arr>').**

3.3.2.2   Transmission loss

Transmission loss is calculated by means of coherent pressure calculations. The alternative transmission loss options "incoherent" and "semi-coherent" attempt to capture less of the detail of the acoustic field, requiring less stringent accuracy and thus lower CPU and RAM capacity with shorter run times. Rays are calculated as Gaussian beams.

Horizontal resolution for the calculations was set to 10 m, while vertical resolution was 1 m. For transmission loss calculations on the paths in the Weddell Sea, vertical resolution was reduced to 2 m as calculations in MATLAB® exceeded memory size.

With ***plotshd('<filename>',1,1,1)*** the transmission loss was plotted as a surface plot. For better comparison of transmission loss data plotting options ***plottld('<filename>',<range>)*** and ***plottlr('<filename',[depth])*** display the transmission loss at a defined range and various depths, respectively.

4. RESULTS

4.1 SOUND SPEED PROFILES

Factors influencing the sound speed profile in the Southern Ocean are primarily the ice coverage and changes in salinity of the layer close to the surface. Profiles obtained by shipborne CTD casts on two expeditions (ANT-XXIX/2 and PS89) exhibit only minor variation between the mooring positions on the Greenwich Meridian south of 60°S (AWI229, AWI230, AWI231 and AWI232, please refer to Figure A.3 in the Appendix).

Sound speed profiles from a float at positions close to 69° S and 27° W show negligible differences between winter and summer data at depths below 200 meters. January (summer) and March (fall) data in Figure 10 (orange and black lines, respectively) exhibit differences of up to 10 m s^{-1} within the about 50m thick surface layer in comparison with the winter (July) and spring (November) data (blue and red lines in Figure 10). Spring and summer sound speed profiles have their sound speed minimum at about 60 m depth, while it is located at the surface in winter. Note that measurements in July and November, as well as one profile in January are truncated at 10 m water depth because the temperature driven ice-algorithm aborted the float's ascend, anticipating ice on the surface. However, with temperatures being constant in that layer at that time, these sound speed profiles can be linearly extrapolated to the surface.
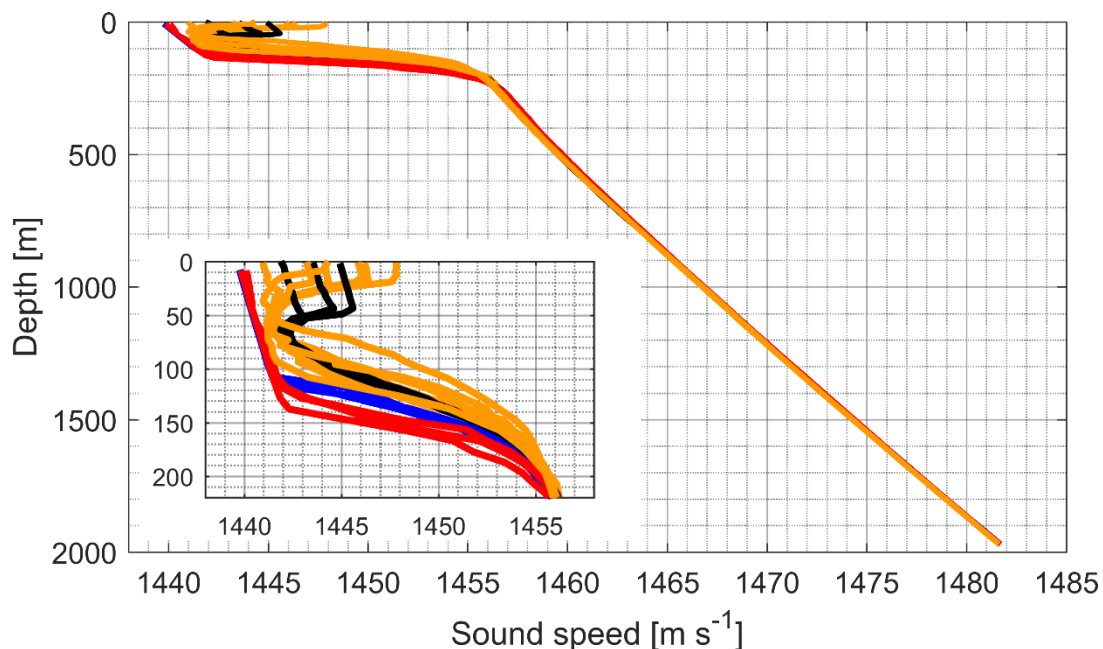
Figure 10: Sound speed profile from float 272 in the Weddell Sea. Values from January (2017 and 2018) in orange, March 2017 in black, July 2017 in blue and November 2017 in red.

Data sampled by CTD data loggers from moorings AWI229 and AWI230 in 2013 was analyzed regarding possible seasonality of the sound speed. The sensors were moored in depths greater than 200 meters. Scrutiny of year-round sound speed data suggests no seasonal pattern at the depths of the moored data recorders. In mooring AWI229 variations ranged to about 3 m s^{-1} at depths greater than 400 m, while in AWI230 sound speed varied by less than 1 m s^{-1} at the same depths (see Figure A.1 and Figure A.2 in Appendix).

As the sound speed profile remains relatively stable throughout the year, an averaged sound speed profile was used as standard for the model input. Nevertheless, to avoid missing any influence of the variations of the sound speed profile in the upper 200m on the propagation, model runs were initiated with four different profile types displayed in Figure 10 (January, March, July and November). Results of the model runs are presented in Chapter 4.5.

4.2 SENSOR DEPTH

Depth records from moored CTD loggers provide information on instrument depth over the deployment period (Figure 11). The result shows that at mooring AWI229 the CTD (nominal depth 718 m) moored 89 meters above the sound source (nominal depth 807) and 251 m above the acoustic recorder (nominal depth 969 m), was suppressed by ocean currents by up to 160 m. A similar change of depth appeared in 2015 (see Appendix Figure A.4). By contrast, instruments moored at the Weddell Sea mooring sites AWI209 in 2013(Figure 11, lower plot) and AWI208 (Figure A.4) did not display any significant variations of deployment depth.
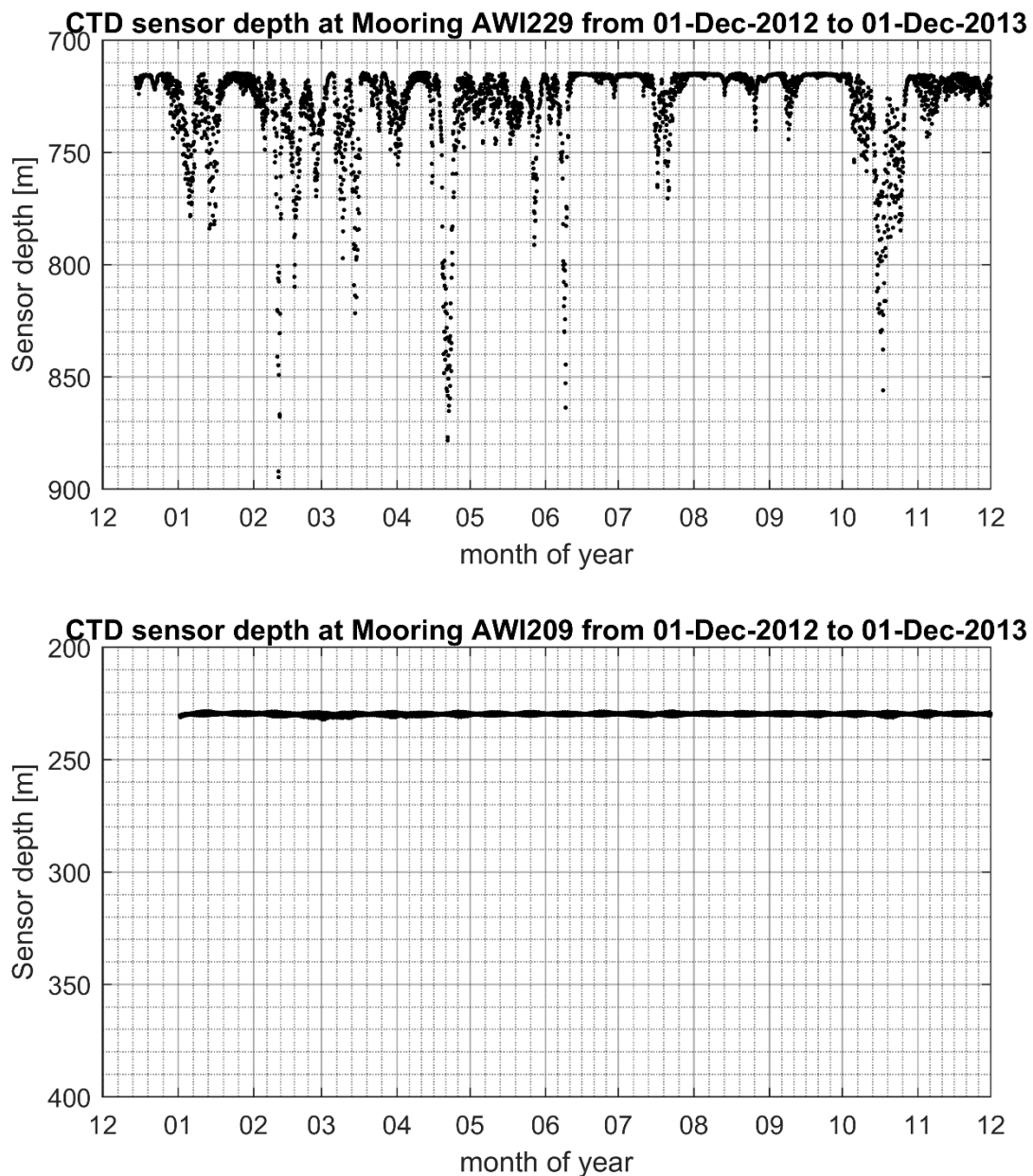
Figure 11: Depth measured by an SM37 CTD logger moored at 718 m depth in AWI229-10 (GM, top) and AWI209-07 (WS, bottom) from December 2012 until December 2013.

4.3 SEA ICE DATA

Weddell Sea

Decrease of sea ice concentration along the great circle in the Weddell Sea between the mooring positions AWI208 and AWI209 started in December 2012. Ice formation commenced in 2013 with the end of March and reached its first maximum with the end of April, with ice thicknesses around 40-50cm. Please note, however, that SMOS ice thickness data is provided only until September 2013. From the beginning of May until the end of September, sea ice thickness in this area exceeds the maximum limit provided by SMOS, implying an ice thickness of 50 centimeters minimum. For a short time in June, ice thickness decreases to values between 40 and 50 cm, after which it returns to the measurements upper limit, potentially exceeding 50 cm.
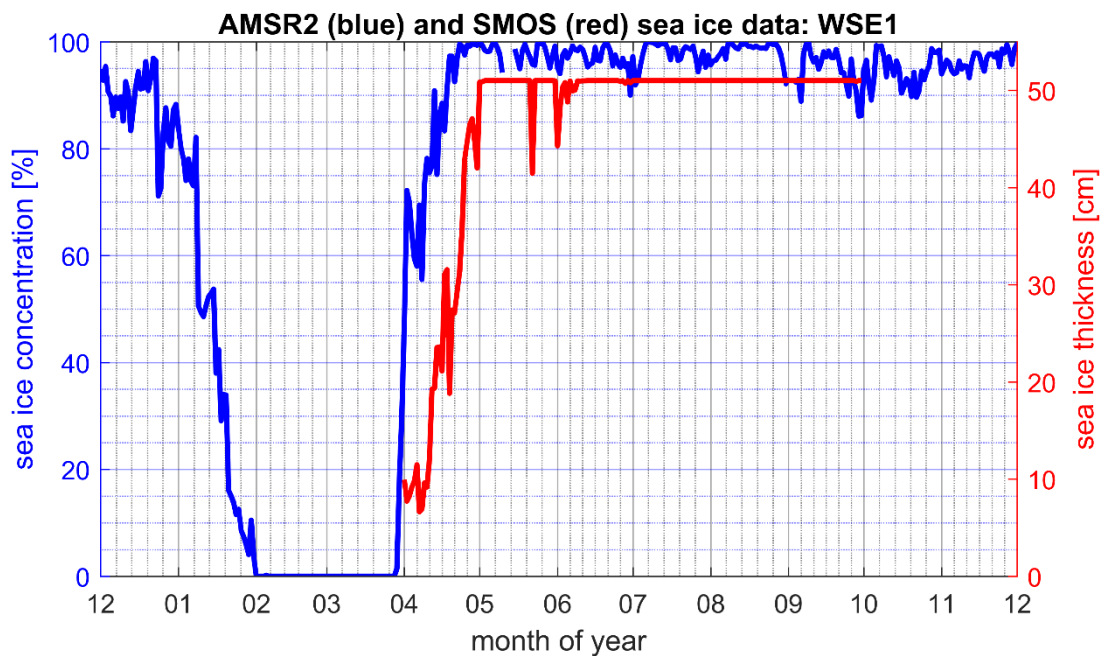
Figure 12: Sea ice concentration (AMSR2 data, blue line) and thin sea ice thickness (SMOS data, red line) along propagation paths in the Weddell Sea in 2013. Data represent path-averaged values.

Greenwich Meridian

The sea ice concentration reaches its first minimum along the great circle between moorings AWI229 and AWI231 on the Greenwich Meridian mid-December in 2012 and in 2015 at the beginning of January. In 2015, sea ice formation starts at the beginning of May in 2013 and mid-April. It reaches its maximum in May, but varies between 80 % and 100 % throughout the winter months. Mean *thin sea ice thickness* data shows an increase from April to May, varying between 40 and 50 cm until August, after which it exceeds the 50cm thickness maximum measurement limit. Generally, *thin sea ice thickness* varies more strongly along the Greenwich Meridian than at the Weddell Sea positions.
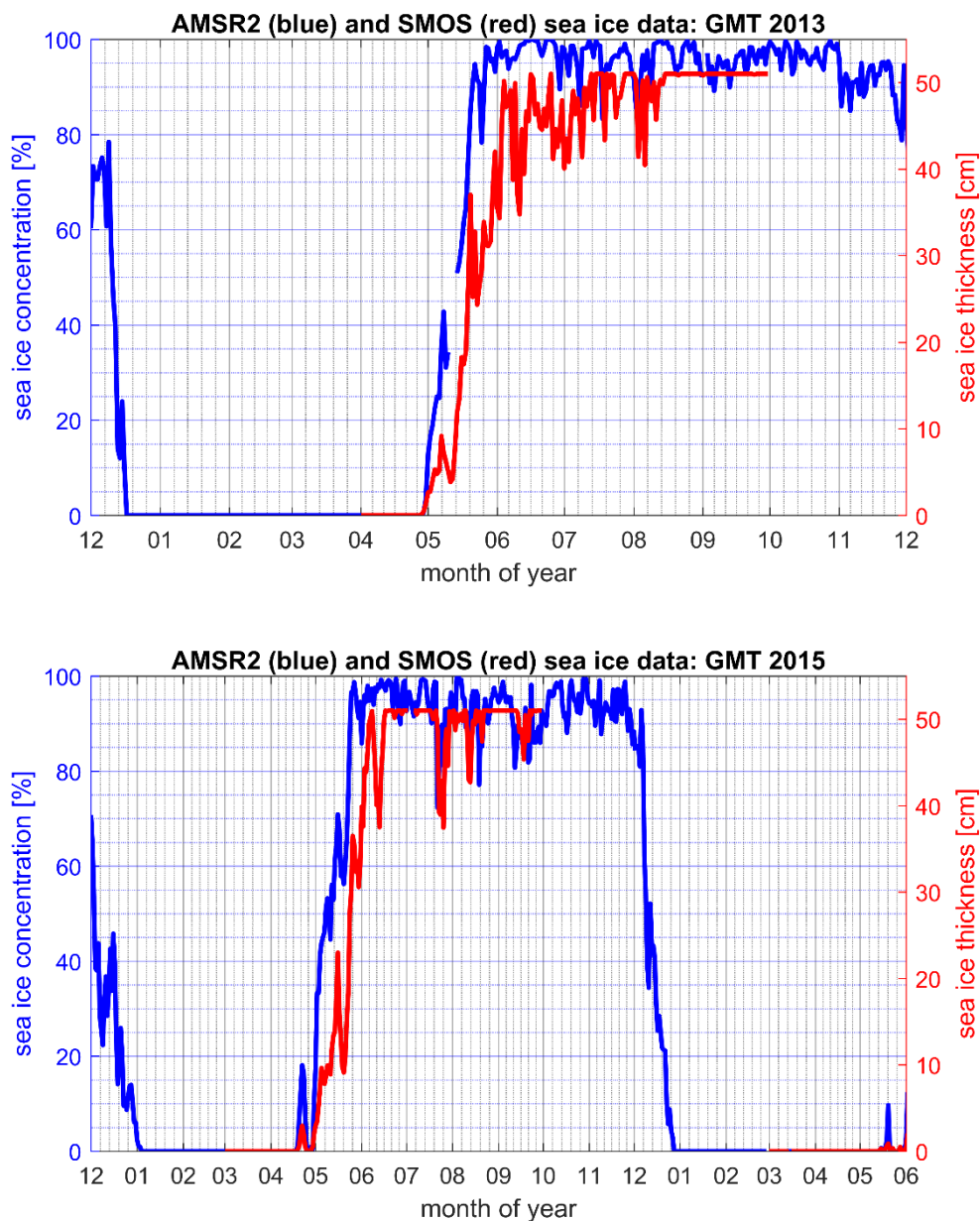
Figure 13: Sea ice concentration *(AMSR2 data, blue line) and* thin sea ice thickness *(SMOS data, red line) along propagation paths GMT along the Greenwich Meridian in 2013 (top) and 2015/2016 (bottom). Data represent path-averaged values.*

4.4 ANALYSIS OF RECORDED RAFOS SIGNALS

4.4.1 *Theoretical calculation of RAFOS signal propagation*

When applying Thorps formula (see chapter 2.2.2.2) to the frequency of interest in this thesis at 260 Hz, the attenuation coefficient is calculated as:

$$\alpha = 0.0426 \text{ dB } km^{-1}$$

For the calculation of geometrical spreading, the formulas from Chapter 2.2.2.1 is applied. For the transition range from spherical to cylindrical spreading *(mean waterdepth)/2* is assumed.

$$TL_{sph} = 10 * \log_{10}\left((\frac{d}{2})^2\right)$$

$$TL_{cyl} = 10 * \log_{10}(r) - 10 * \log_{10}\left(\frac{d}{2}\right)$$

$$a = r * \alpha$$

$$TL_{total} = TL_{sph} + TL_{cyl} + a$$

Path ID	Range r [km]	Mean water depth d [m]	TL_{sph} - spherical spreading [dB re 1µPa]	TL_{cyl} - cylindrical spreading [dB re 1µPa]	a - attenuation [dB re 1µPa]	TL_{total} * [dB re 1µPa]
			Transmission Loss			
WSW	432.5	4800	23	68	18	109
WSE1	432.5	4800	23	68	18	109
WSE2	432.5	4800	23	68	18	109
GMS	53.4	3819	15	66	2	83
GMN	226.8	4144	20	66	10	96
GMT 2013	280.1	4108	21	66	12	99
GMT 2015	284.9	4082	22	66	12	100

Table 5: Calculated transmission loss for all propagation paths.) without boundary interaction.*

4.4.2 Analysis and comparison of single RAFOS signals

For every sound snippet, time series of instantaneous correlation heights, sound pressure level and a spectrogram were displayed. The top panel in the following figures (Figure 14 to Figure 16) show the time series of instantaneous correlations, normalized to the overall maximum correlation for the respective pairing and scaled from 0 to 100. The middle panel represents the windowed RMS received level of the bandpass filtered data. The spectrogram of the bandpassed file data is displayed in 'parula' colormap (bottom panel).

Strong variations in signal levels are observed between subsequent days (Figure 14and Figure 15).On some days parts of the signal are missing, while on other days the signal is superposed by broadband impulses (Figure 16).
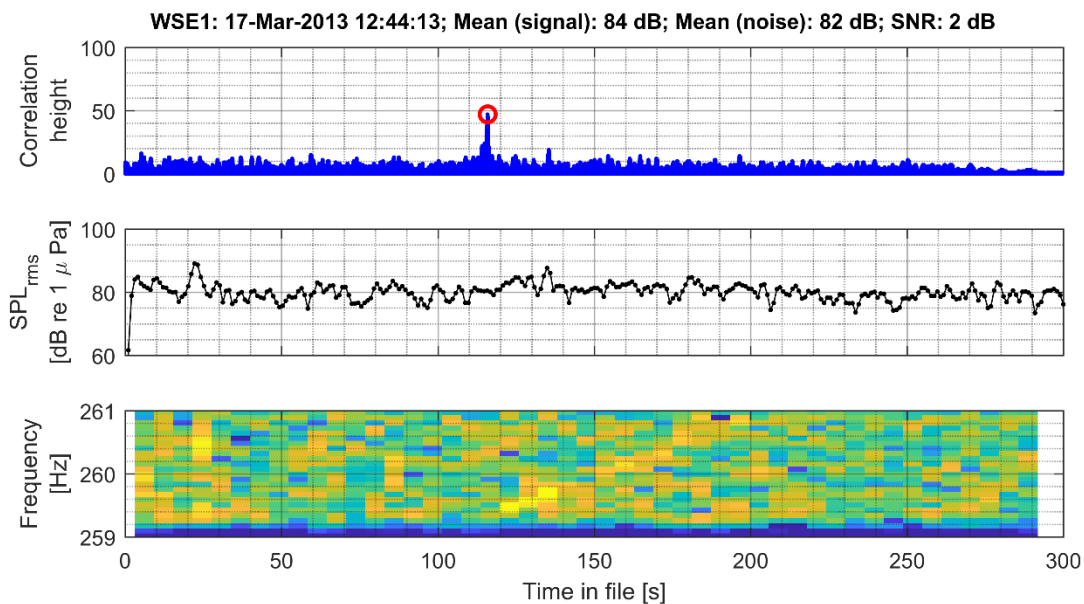
Figure 14: Analysis of single received signals from WSE1. Snippet 1 of 2 from subsequent days. While the noise level is higher and RAFOS signal is only partly visible in the upper spectrogram, the signal is clearly discernable one day later in the spectrogram in Figure 15.
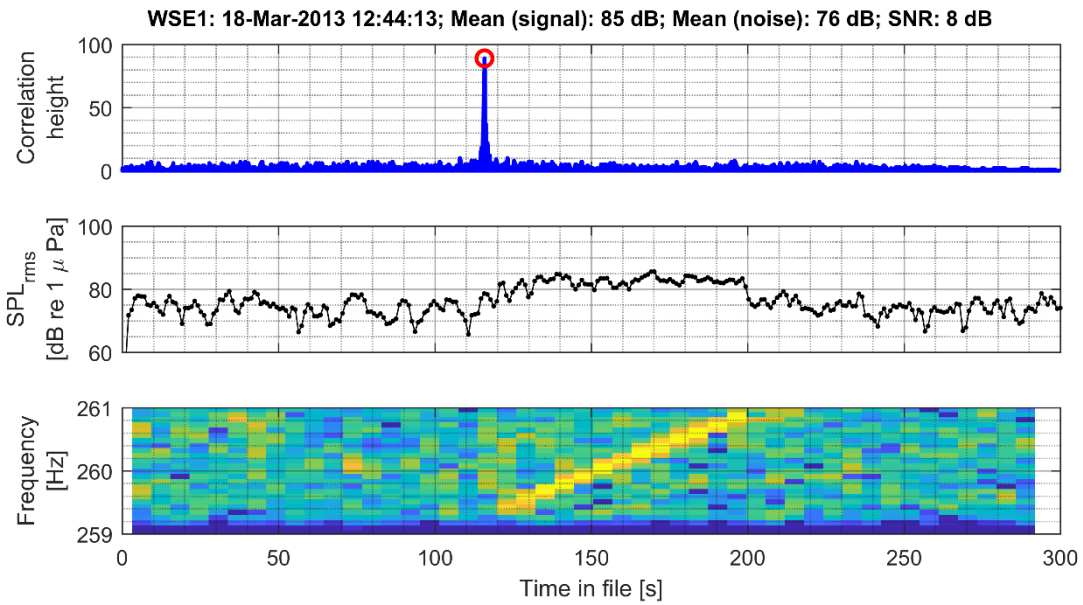
Figure 15: Analysis of single received signals from WSE1. Snippet 2 of 2 from subsequent days. The signal is clearly discernable in the spectrogram, while it is only partly visible in Figure 14.
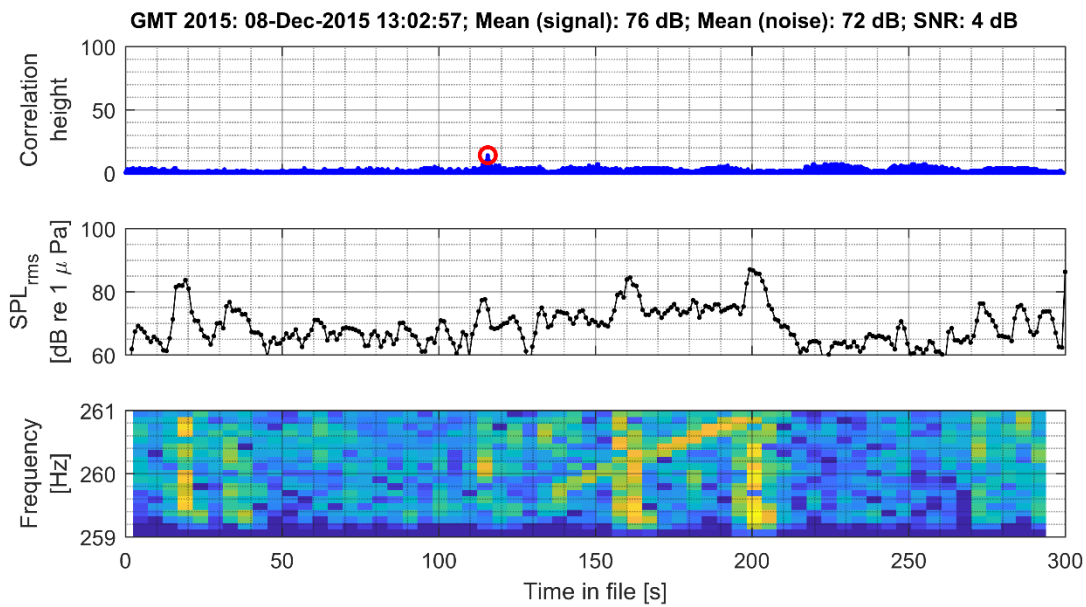
Figure 16: Analysis of single received signal from GMT 2015. The broadband pulses lie within an otherwise clearly discernable signal.

37

4.4.3   Analysis of different propagation paths

4.4.3.1   Weddell Sea Moorings

The distance between Weddell Sea moorings AWI208 and AWI209 is approximately 430 km. Each mooring hosted a sound source at about 800 m depth. AWI209 contained one acoustic recorder at about 1000 m depth (Data from WSW), while AWI208 contained two recorders; one at around 1000 m (Data from WSE1), and one at about 2500 m water depth (Data from WSE2).For further details on the paths nomenclature please refer to Chapter 3.1.1.

Figure 17 and Figure 18 summarize the results for the acoustic propagation of the RAFOS signal for path WSE1.

Figure 17 serves to examine the relation of the correlation height, which is color-coded identically in all sub-plots of this figure, to the time-of-arrival, the received sound pressure level of the RAFOS signal, ambient noise, as well as to the resulting SNR and transmission loss.

The quality of time-of-arrival from the correlation is high throughout the ice-free period in Antarctic summer and appears to degrade during the ice-formation from April to the beginning of June (panel 1). After May, *ToA* starts to be distributed rather randomly around the expected *ToA*. This coincides with the drop of correlation height presented in panel 2, which reaches its minimum between May and June with values close to 0.

Panel 4 shows the received sound pressure level of the RAFOS signal, which reaches its lowest value two months after average ice concentration along the path reaches values between 95 % - 100%. SPL decreases from values between 80 and 85 dB re 1µPa at times with no sea ice cover to values as low as 65 dB re 1µPa during ice cover. Analog to the drop of sound pressure level, transmission loss for the signal increases by over 10 dB between ice-free and ice covered seasons (panel 3). The ambient noise level in panel 5 drops concurrently with the RAFOS signal level, however the resulting SNR in panel 6 changes from mainly positive values with up to 7 dB before the ice forms, to values around 0 dB or slightly negative during ice coverage.
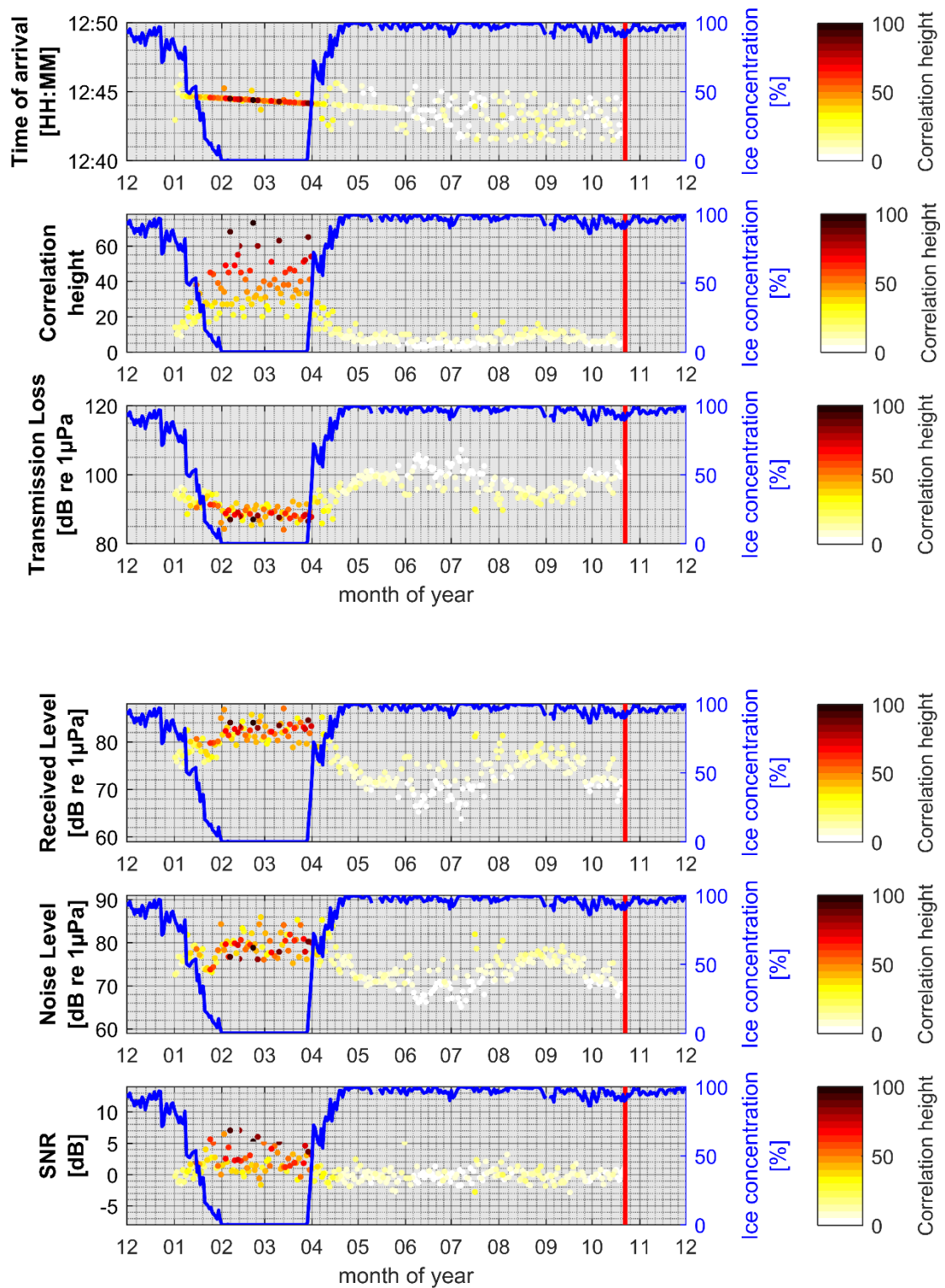
Figure 17: Time series of RAFOS signal reception for the Weddell Sea East 1 (WSE1) path. Top to bottom: 1) ToA of (corrected) RAFOS signal, 2) correlation height, 3) transmission loss , 4) filterd RMS SPL of signal, 5) filterd RMS SPL of noise in same band as the signal, 6) and the SNR. Sea ice concentration is plotted as blue line in all subplots, correlation height is color coded (see colorbar on the right) The end of the recordings is marked with a red line.

Figure 18 depicts the relation between *ToA* quality and the same parameters as in the previous figure. The upper panel 1 in Figure 18 underlines the degradation of the detection quality. In June, relative *ToA*s exhibit a stronger scatter around the line of expected *ToA*. From July until the end of the available recordings, clustering of detections with low *relative ToA*s is not noticeable. Nevertheless, plausible *ToA*s are delivered by the correlator until the end of May, when the transmission loss had already increased by 10 dB. Because of the poor agreement with the expected *ToA* and hence the high probability of false positive detections, data with a deviation greater than 5 s from the estimated *ToA* were set to NaN for further calculations (see Chapter 3.2.3). In consequence, data after June, will not be regarded in the following evaluation.

Panels 2 trough panel 6 underline the behavior of the respective parameters presented in Figure 17.

Results from paths WSW and WSE2 show the same pattern as WSE1 with only minor differences regarding the absolute values. All additional plots are included in the Appendix.
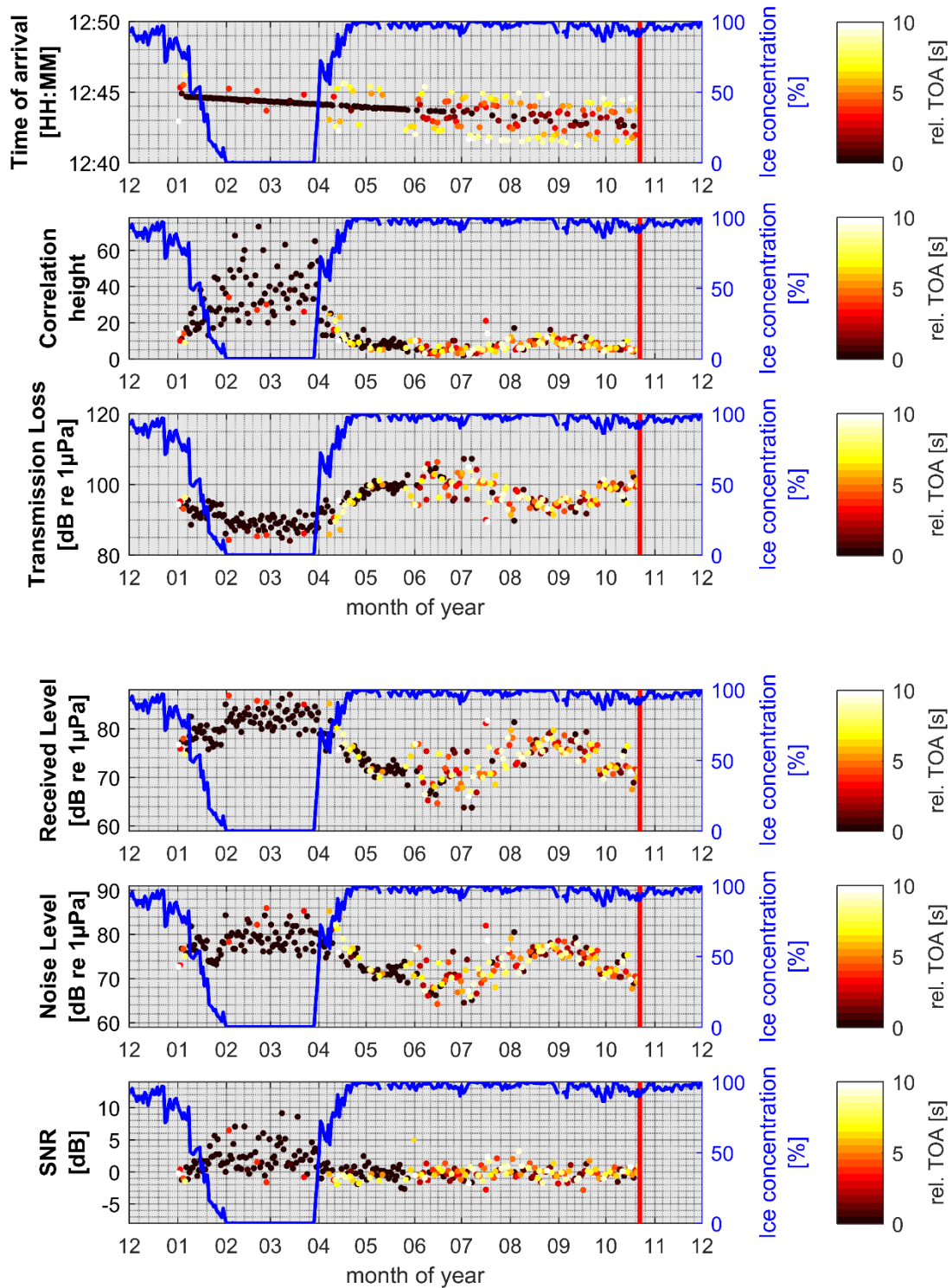
Figure 18: Time series of RAFOS signal reception for the Weddell Sea East 1 (WSE1) path. Top to bottom: 1) corrected RAFOS signal ToA at recorder position, 2) correlation height, 3) transmission loss in dB, 4) RMS SPL of the filtered received signal in the acoustic recorder, 5) the RMS SPL in dB of the noise in same band as the signal, 6) and the SNR in dB. Sea ice concentration is plotted as blue line in all subplots, relative ToA is color coded (see colorbar on the right) The end of the recordings is marked with a red line.

The resulting transmission loss of all Weddell Sea propagation paths is shown in Figure 19. As previously described, only data points with relative ToA < 5 s are included in the calculations. Therefore, data later than June was neglected, as described earlier. The behavior of all three paths regarding the increase of transmission loss during ice formation is similar. 10-day averages of transmission losses for WSE1 (panel 1) and the opposite direction WSW (panel 2) increase from about 89 dB to 104 dB and 90 dB to 110 dB, respectively. Transmission loss along WSE2 (panel 3), featuring the recorder at 2516 m nominal depth increasing from 88 dB to a maximum of 98 dB. Standard deviation for the values of WSE2 is generally higher than in WSE1 and WSW.
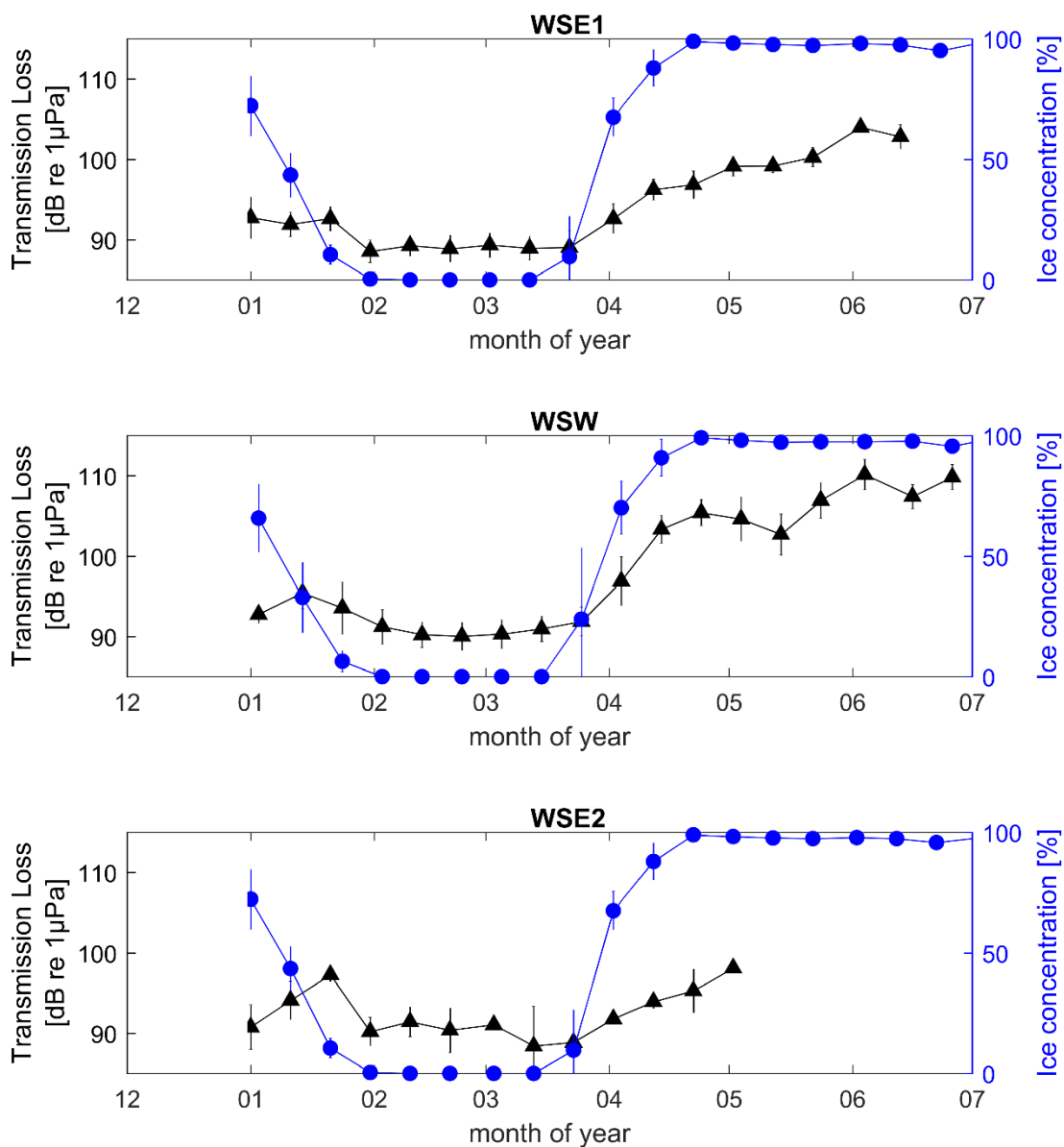
Figure 19: Comparison of transmission loss along paths WSW, WSE1 and WSE2. Black triangles represent 10-day averages with the standard deviation, while blue markers represent 10-day average of the mean ice concentration along the path.

The comparison of all three paths reveal, during times of sea ice presence, higher transmission losses for the westerward path WSW than for both eastward paths (Figure 20).
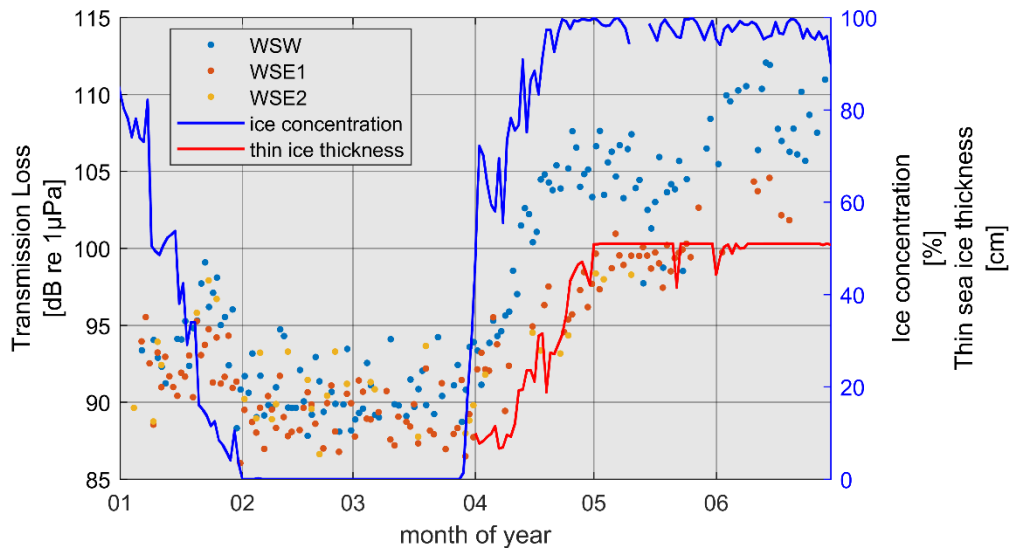
Figure 20: Comparison of transmission loss of received signal on paths in the Weddell

Correlation plots in Figure 21 reveal a clear correlation between the increasing sound pressure level of the received signal and increasing correlation height (top left panel). When regarding the relative time-of-arrival data in the panel on the lower left, differences between WSE1 and WSW are apparent. While *rel. ToA* appears to be decreasing with better correlations for WSE1, data suggests the opposite for WSW. Measured noise levels (upper right panel) correlate with correlation height in a similar fashion as the received RAFOS signal level, resulting in rather small differences of SNR (lower right panel). Nevertheless, improving SNR seems to influence correlation heights positively, even though a high variability in the data is present.
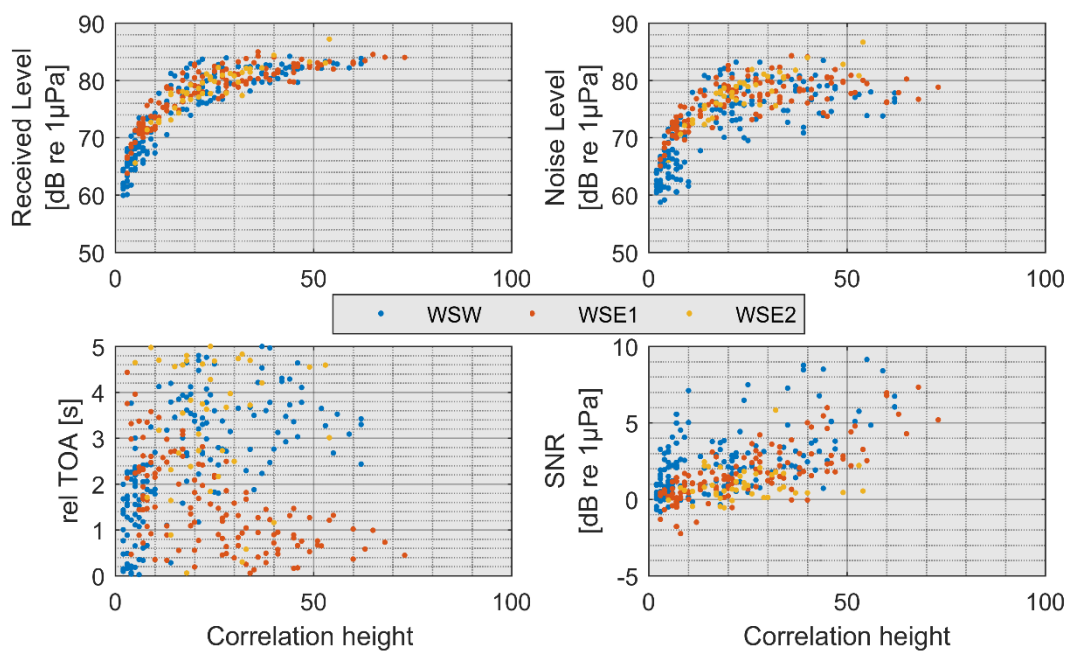
Figure 21: Correlation of different parameters with correlation height. Top left: Received level of RAFOS signal, top right: noise level, bottom left: relative ToA, bottom right: SNR.

43

Signal quality decreases with increasing ice concentration and *thin ice thickness*, as presented in Figure 22. Sound pressure level of the received signal (upper left panel), as well as correlation height (upper right panel), display a distinct degradation with increasing ice. Within the limits of ±5s, a correlation between *relative ToA* and ice concentration or *thin sea ice thickness* appears not to exist (lower left panel). SNR (lower right panel) is higher when the ice concentration is low, for ice thickness no clear relationship could be determined.

a)
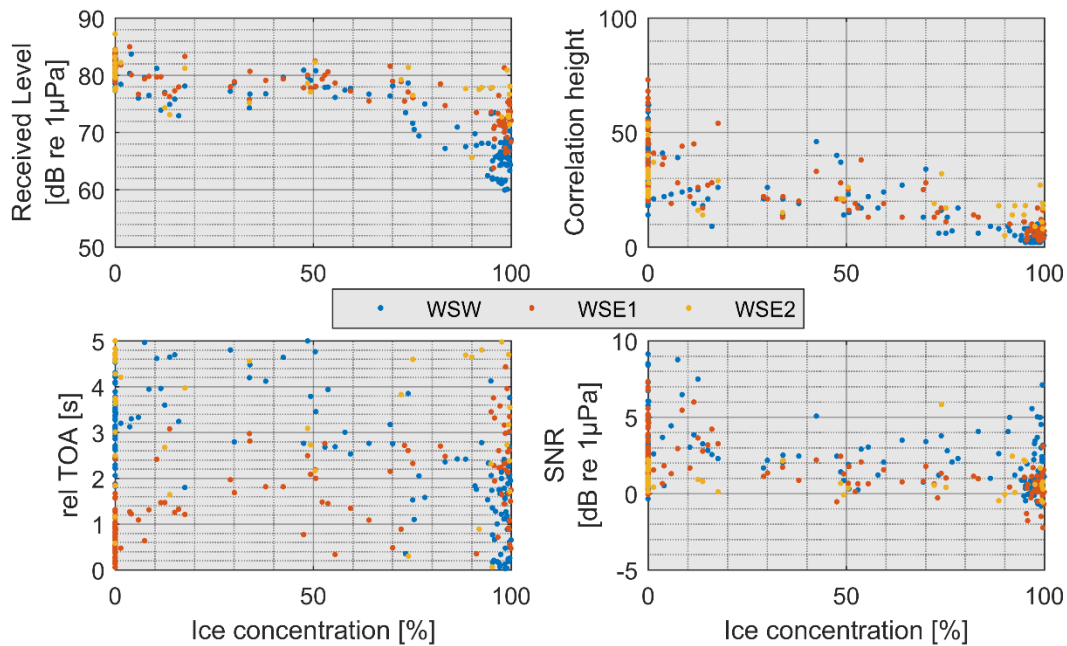
b)
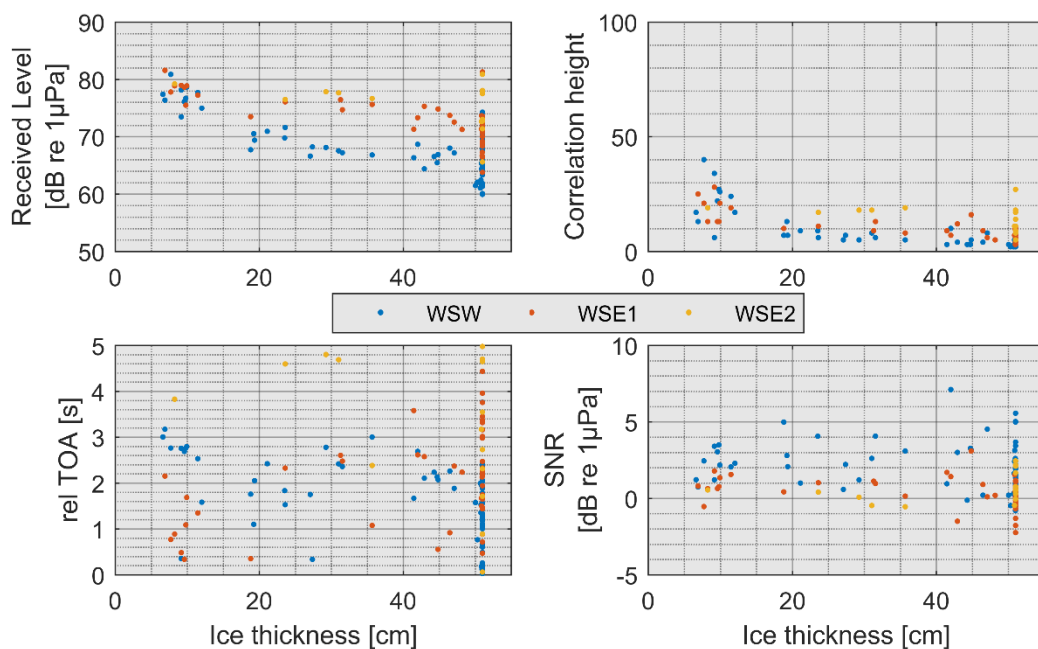
Figure 22: Correlation of different parameters with averaged sea ice concentration in a) and averaged thin sea ice thickness in b), along propagation path. Top left: received level of signal, top right: correlation height, bottom left: transmission loss, bottom right: SNR

4.4.3.2 Greenwich Meridian

The distance between Greenwich Meridian moorings AWI231 and AWI229 is approximately 280 km. Each mooring hosted a sound source at nominally 800 m depth. In addition, AWI229 featured one acoustic recorder at about 1000 m depth. For more information on the analyzed paths, please refer to Chapter 3.1.1.

Figure 23 and Figure 24 summarize the results from the acoustic propagation of the RAFOS signal from analyzed path GMT 2015 on the Greenwich Meridian analog to the analysis of WSE1 in the previous chapter.

Data concerning path GMT 2015 comprise almost 18 months, including an entire winter season. Results show that the behavior of the signal level and resulting correlation height is similar to the one described for the Weddell Sea.

Figure 23 displays the relation of the correlation height, which is color-coded in the plots, to time-of-arrival, the received level of the RAFOS signal, ambient noise level, resulting SNR, and transmission loss. Sea ice concentration is plotted alongside these parameters.

Similar to the results from the Weddell Sea, the quality of time-of-arrival from the correlation is high throughout the ice-free period in Antarctic Summer. In case of path GMT 2015 there is no significant change of *rel. ToA* during ice-covered periods (panel 1). While correlation height drops to values between 0 and 20 when ice covers the surface, ToAs remain equally good as in times without ice cover. Correlation heights before ice formation are highly variable with values from 10 to 60 (panel 2). Lowest correlations are reached between August and December. Accordingly, sound pressure levels of the received signal (panel 4) and noise (panel 5) decrease slowly from the start of ice formation in the beginning of May until August. Initial sound pressure levels of the received RAFOS signal range between 80 and 85 dB re 1µPa at times without sea ice cover, decreasing to values varying around 70 to 75 dB re 1µPa during ice-covered periods. RL recover quickly in the melting season, increasing to their original values within one month in December. Similarly, transmission loss of the RAFOS signal increases by over 10 dB between ice-free and ice covered seasons. In contrast to the Weddell Sea mooring, SNR along GMT 2015, presented in panel 6, keeps within limits of 0 to 10 dB.

Panel 1 in Figure 24 underlines the fact that *ToA* from the correlation is of high accuracy throughout all ice conditions. A closer look at the first plot with *ToA* over time suggests there might be a second set of valid *TOA*s, possibly from another sound source further afield.
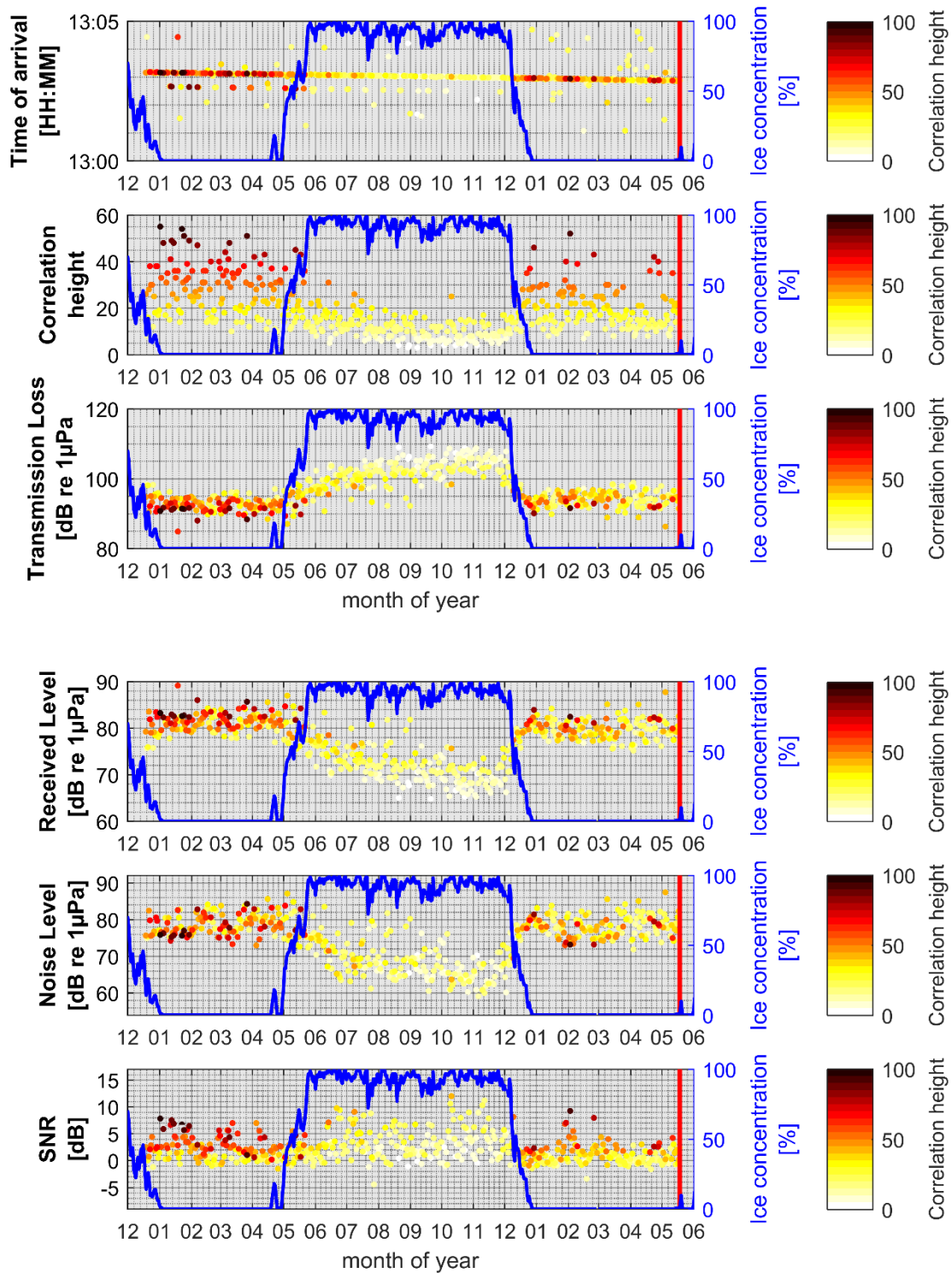
Figure 23: Time series of RAFOS signal reception for the Greenwich Meridian Total 2015 (GMT 2015) path. Top to bottom: 1) ToA of (corrected) RAFOS signal, 2) correlation height, 3) transmission loss , 4) filtered RMS SPL of signal, 5) filterd RMS SPL of noise in same band as the signal, 6) and the SNR. Sea ice concentration is plotted as blue line in all subplots, correlation height is color coded (see colorbar on the right) The end of the recordings is marked with a red line.
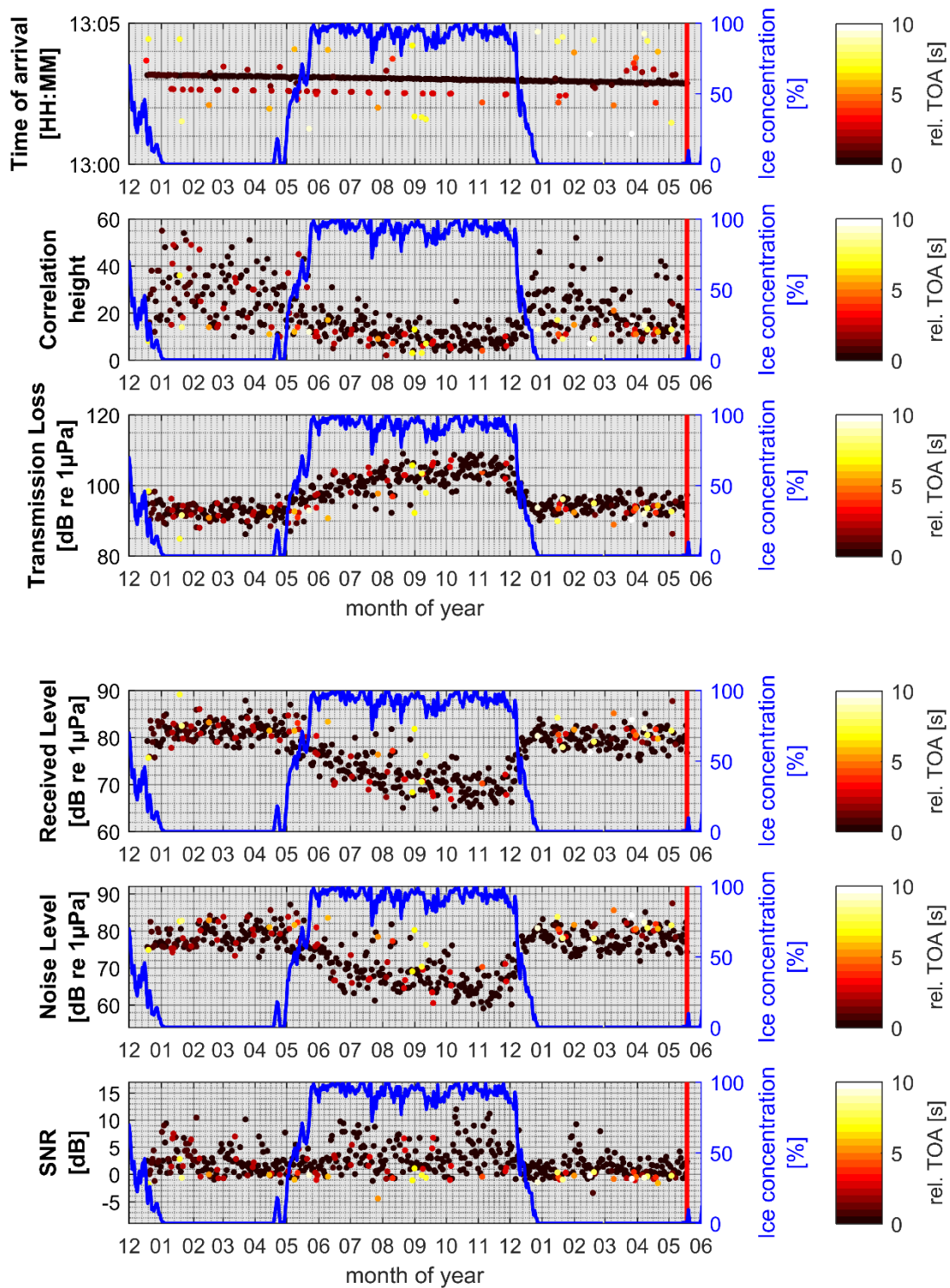
Figure 24: Time series of RAFOS signal reception for the Greenwich Meridian Total 2015 (GMT 2015) path. Top to bottom: 1) corrected RAFOS signal ToA at recorder position, 2) correlation height, 3) transmission loss in dB, 4) RMS SPL of the filtered received signal in the acoustic recorder, 5) the RMS SPL in dB of the noise in same band as the signal, 6) and the SNR in dB. Sea ice concentration is plotted as blue line in all subplots, relative ToA is color coded (see colorbar on the right) The end of the recordings is marked with a red line.

Figure 25 displays 10-day averages of the correlation height, *rel. ToA*, signal level in the signal band, SNR and transmission loss. Blue markers mark the 10-day averages of mean sea ice concentration along the path. A temporal correlation between ice formation and signal decrease in panel 1, as well a deterioration of correlation quality in panel 3 can clearly be recognized in the data. Interestingly, *rel. ToA* in panel 2 seems to improve with growing sea ice. Received signal levels before ice formation range at around 80-82 dB and drop by about 7 dB within the first two months of ice formation, to continue decreasing to about 70 dB. SNR, shown in panel 4, appears to be slightly throughout times with ice cover.
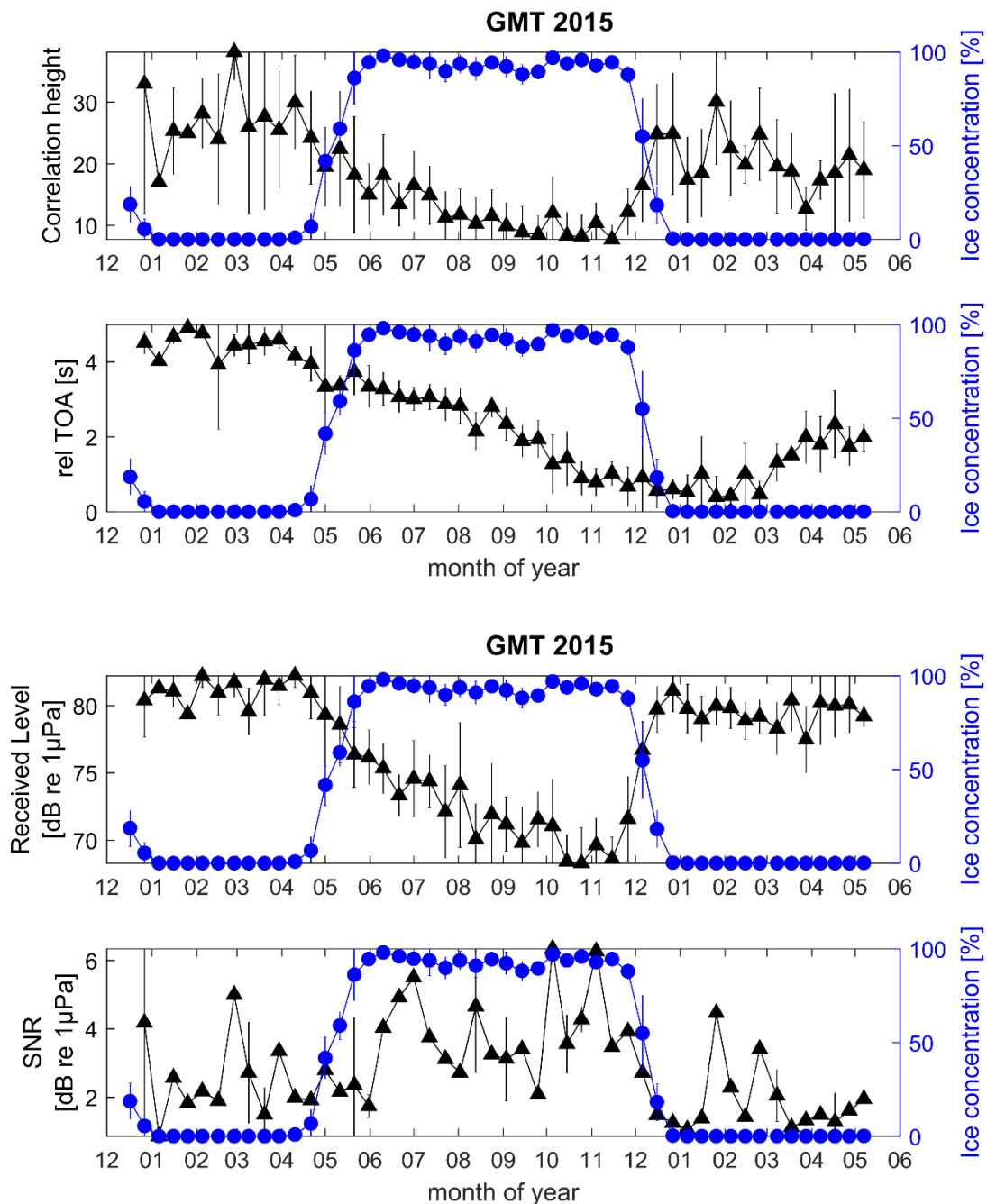
Figure 25: Compilation of correlation height, relative ToA, RL and SNR (black marker) for GMT 2015 in comparison to AMSR2 ice concentration data (blue marker). Markers represent the 10-day averages with standard deviation.

Comparing data from 2013 in Figure 26, differences between path GMN and GMS can be observed. On path GMN, the longer (228 km), northern part on the Greenwich Meridian, received levels of the RAFOS signal decrease clearly by over 7 dB (panel 1). The corresponding SNR, shown in panel 2, increases by about 5 dB during ice formation, reaching its maximum in June. It then decreases to initial values around 6 dB until the end of July. The 10-day average of the received level on the shorter path GMS (53 km) in panel 3 appears to only temporarily increase in April and decreases when the maximum ice coverage is reached. Standard deviations for the received level in GMS is significantly higher than on any other path. Panel 4 shows a significant increase in SNR on path GMS by up to 11 dB during the ice-covered period (to the extent covered by the data).
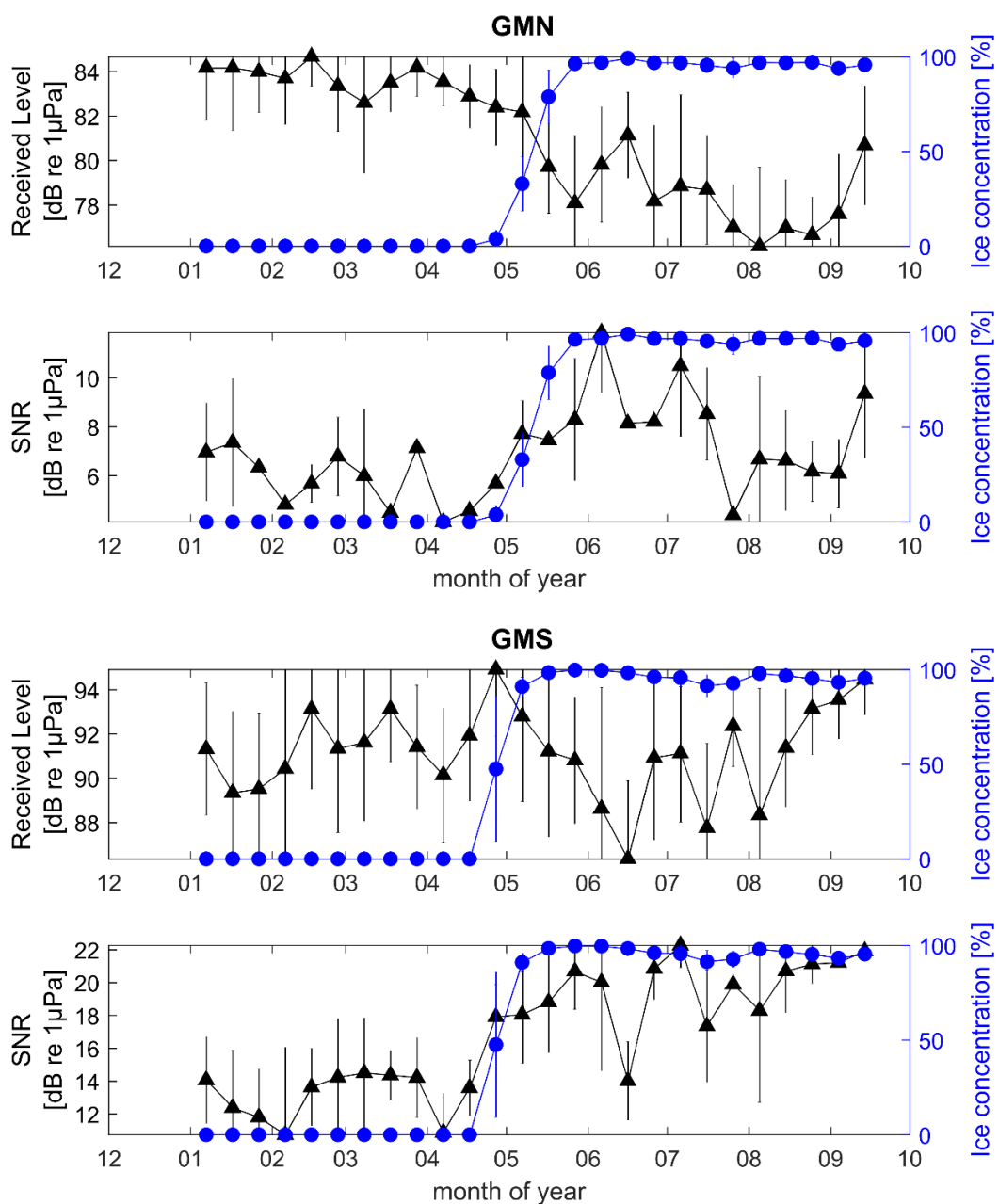
Figure 26: Comparision of RL and SNR (black marker) for GMN and GMS in comparison to AMSR2 ice concentration data (blue marker). Markers represent the 10-day averages with standard deviation.

Data on transmission loss of the year 2013 in Figure 27 shows a similar pattern for GMN and GMT 2013 (upper plot). While transmission loss varies around 90 dB during the ice-free period, it starts increasing with ice formation in May. For GMT 2013 the increase continues until the end of recordings at the end of July. On GMN transmission loss appears to be stable at values around 97 dB until recording ended in September. In contrast, ice coverage seems to influence transmission loss along GMS only insignificantly. The increased transmission loss on the Greenwich Meridian in 2015 prevails until the ice starts melting (lower plot). Therefore, it is not possible to determine whether GMT 2013 would reach the same level of transmission loss as GMT 2015. Nevertheless, levels were similar for the same time of the year.
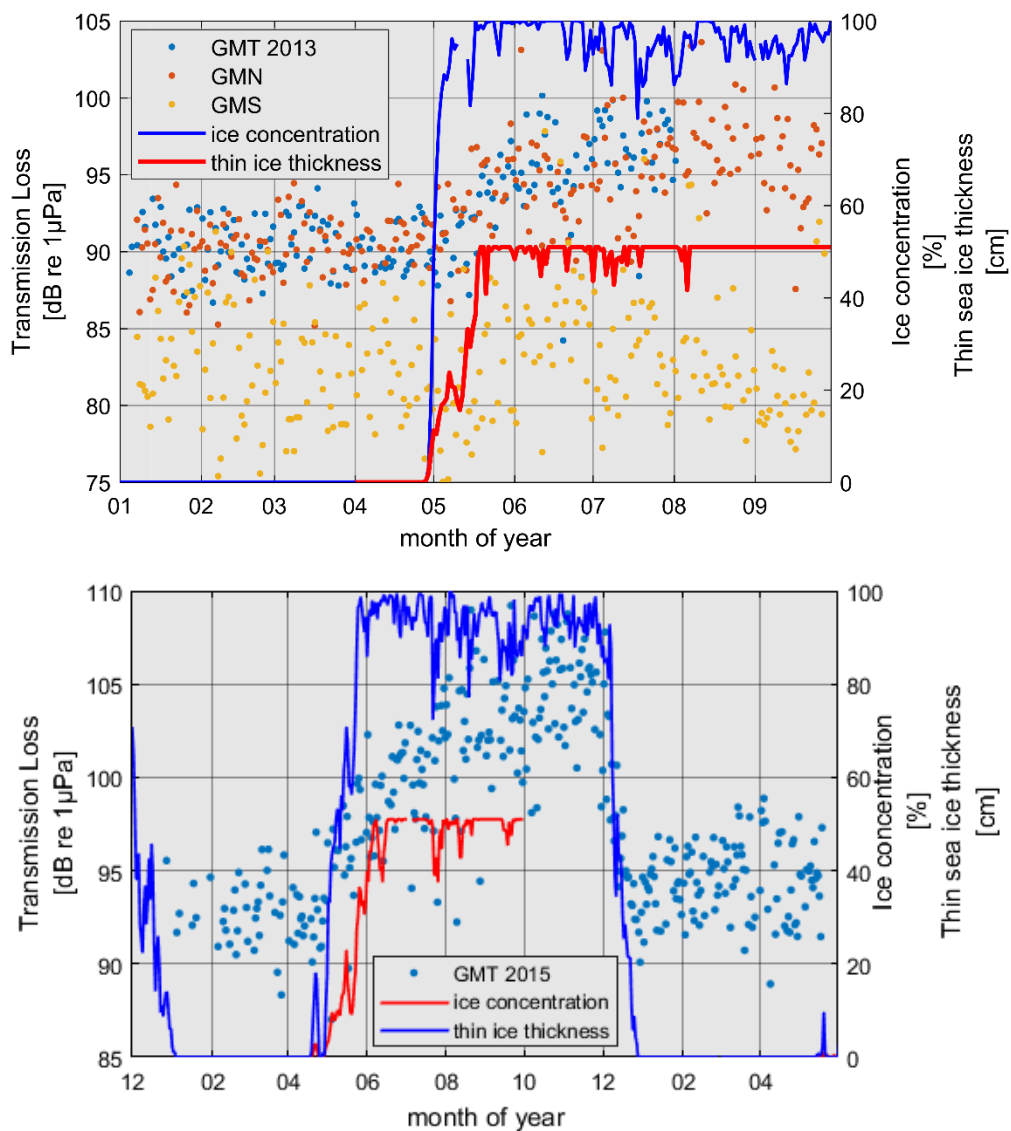
Figure 27: Transmission loss along all analyzed propagation paths: top: Greenwich Meridian in 2013, bottom: Greenwich Meridian in 2015, lower left: Weddell Sea

Figure 28 presents 10-day averages of transmission loss for propagation paths along the Greenwich Meridian, including their standard deviation. Transmission loss along GMT 2015 increases continuously from end of April to November by over 10 dB, while ice concentration along the propagation path varies between 80 % and 100 % (panel 1). Transmission loss drops to values of around 95 dB from end of November to beginning of January. It is therefore slightly higher than TL before the ice season, when it was below 95 dB. Two years earlier in 2013, transmission loss increases until July, when recordings ended (panel 2). By then the increase was nearly 8 dB. On path GMN (panel 3), the northern part of GMT 2013 and, with a length of 228 km, shorter by 53 km, transmission loss increase is similar to GMT 2013. GMS compared to the other three paths displays only insignificant changes in the transmission loss with high standard deviations (panel 4).
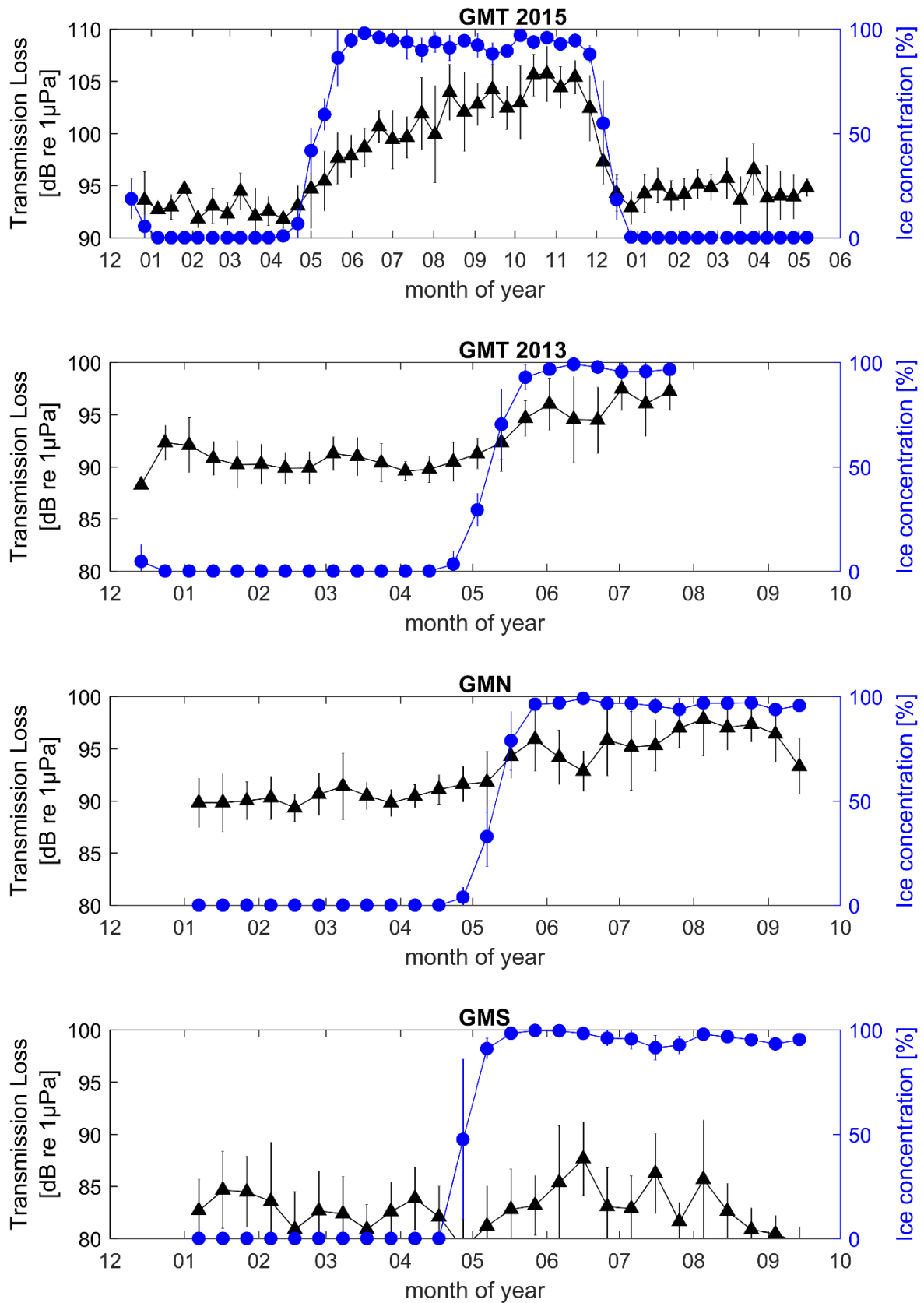
Figure 28: Transmission losses for all analyzed propagation paths on the Greenwich Meridian (black triangle) and AMSR2 ice concentration data (blue marker). Markers represent 10-day averages with standard deviation.

The top left panel in Figure 29 reveals a clear relationship between correlation height and the SPL of the received signal. With increasing sound pressure level correlation quality increases.

Higher noise levels were present when better correlation results were achieved for both GMT paths. On paths GMN and GMS, however, noise level appear to vary strongly between 70 and 80 dB, even when better correlations were achieved (upper right panel). This results in better signal to noise ratios for propagation paths GMN and GMS (lower right panel).
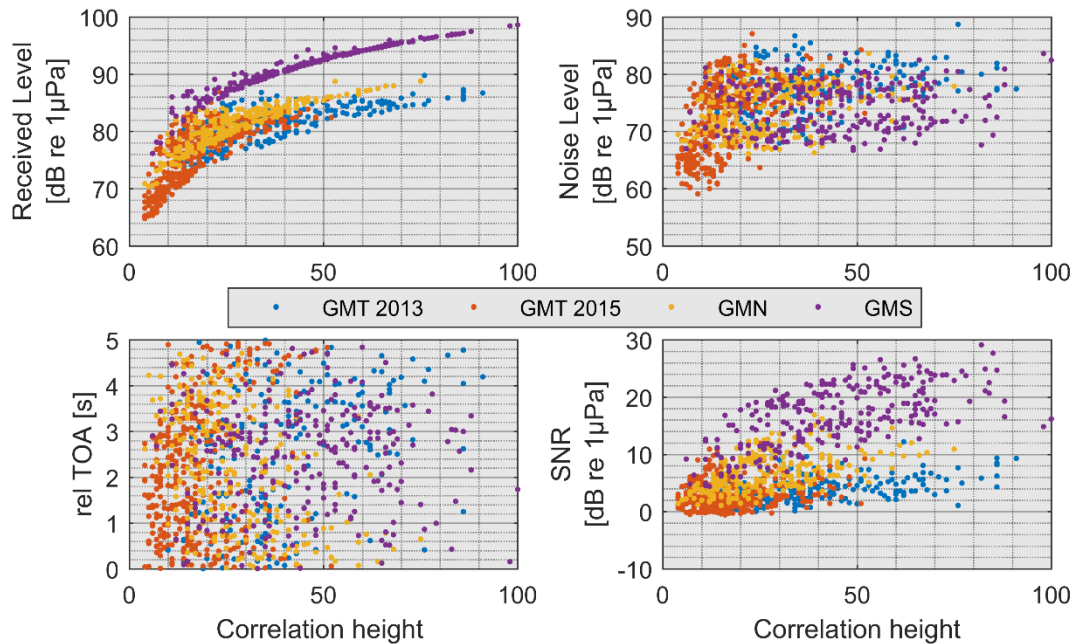
Figure 29: Correlation of different parameters with correlation height. Top left: Received level of RAFOS signal, top right: noise level, bottom left: relative ToA, bottom right: SNR.

Comparable to the data from the Weddell Sea, signal quality decreases with increasing ice concentration and ice thickness (Figure 30, upper left panel). Probably due to the short distance of 53 km, GMS poses an exception, with little dependency of the signal levels on ice coverage. On the other paths, sound pressure levels of the received signal as well as correlation height (upper right panel) display a distinct degradation with increasing ice. Because of the stability of signal levels and decreasing noise levels during ice formation, SNR improves on path GMS with increasing sea ice concentration (lower right panel). Higher SNR values correlate with lower ice concentrations, in case of the ice thickness, no clear connection could be determined. Similar to the Weddell Sea data, a correlation between rel. *ToA* and ice concentration or *thin sea ice thickness* appears not to exist.

a)
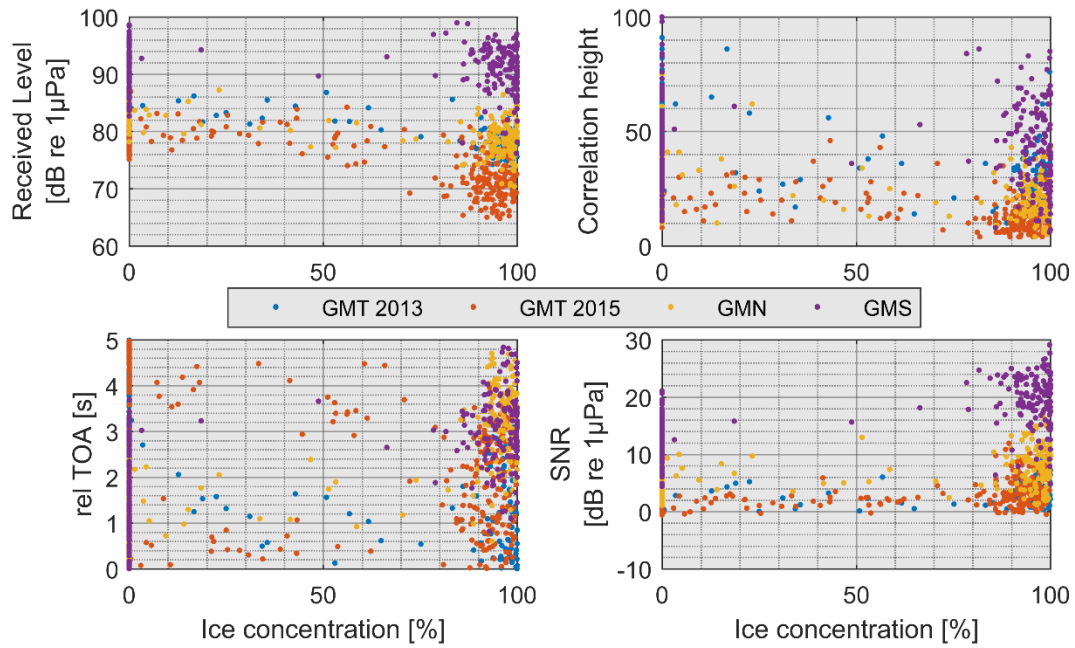
b)
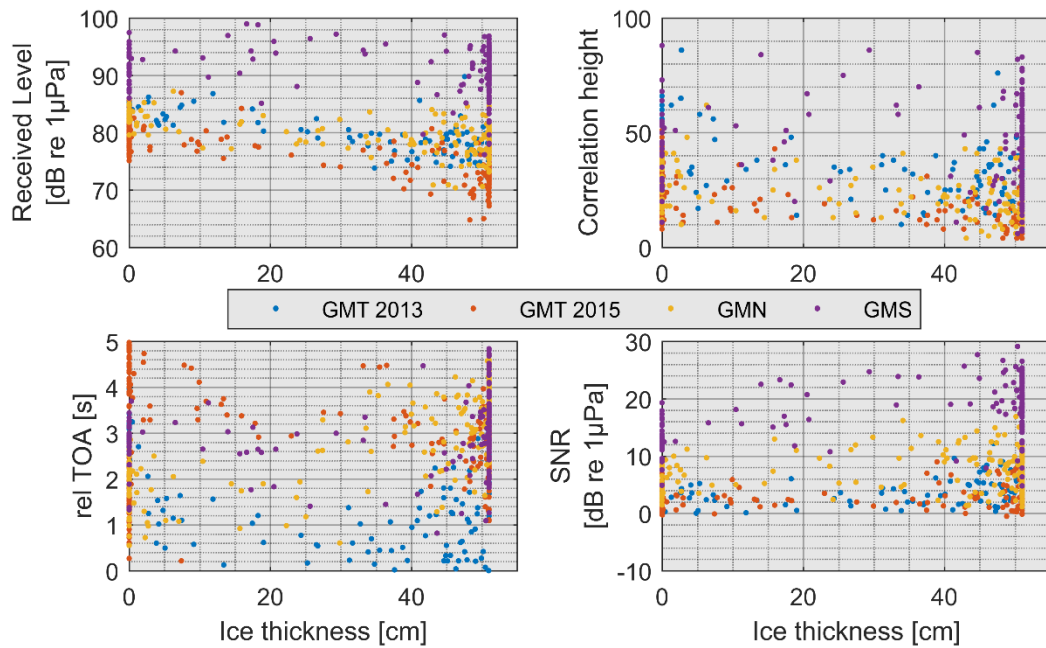
Figure 30: Correlation of different parameters with averaged sea ice concentration in a) and thin sea ice thickness in b), along propagation path. Top left: received level of signal, top right: correlation height, bottom left: transmission loss, bottom right: SNR.

4.5 BELLHOP RAYTRACING OUTPUT FOR RAFOS SIGNAL PROPAGATION

Eigenray plots for the different paths show multiple bottom and surface bounces for each path with the number of displayed rays being set automatically by BELLHOP. Figure 31 and Figure 32 show Eigenray plots as well as the travel time and transmission loss for GMT 2015 and GMS, respectively. Calculations are based on the assumption of an ice free surface with adjacent vacuum. Eingenray calculation include realistic bathymetry data. Red lines indicate rays without any bottom bounce, while black lines indicate rays with bottom and surface bounces. All model outputs reveal the lack of a direct path (i.e. without bounces). GMS, as the shortest of all paths (53 km), contains Eigenrays which experience a single surface bounce only, being the lowest number of boundary contacts for all analyzed paths. Rays transmitted by the source at greater angles interact with the interfaces at steeper angles, leading to multiple surface and bottom bounces. This, results in longer travel paths and thus longer travel times. A consequence of the longer travel paths and the increase in number of bounces are higher transmission losses. Stem plots for GMT 2015 show transmission losses of 100 dB – 110 dB at travel times of 195 ±1 s for paths with surface contact only, while paths including bottom bounces experience transmission losses of 110 dB – 150 dB at travel times varying from 193 s to 207 s.
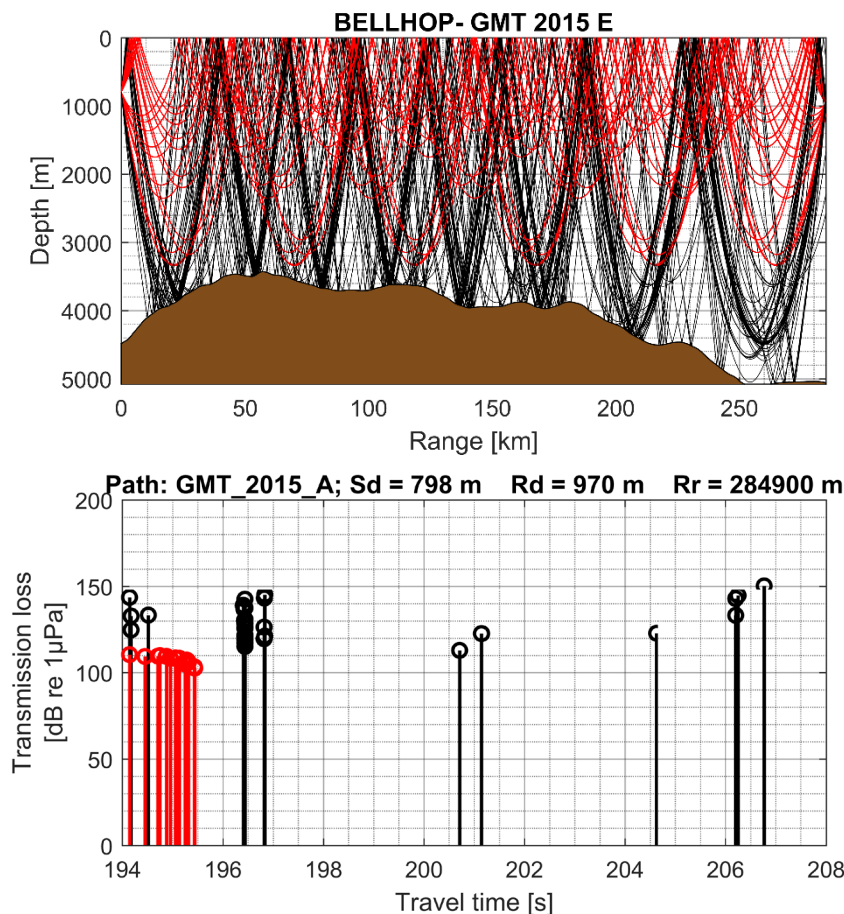
Figure 31: Exemplary raytracing plot of Eigenrays (top) and transmission loss over travel time (bottom) for GMT 2015. In both plots: Rays without any bottom bounce in red, bottom and surface bounces in black. Source depth (Sd) is 798 m, recorder depth (Rd) is 970 m and range (Rr) is 284.9 km.

Results for path GMS show a travel time of 36.5 s with transmission losses of 90 dB for rays without any bottom bounce, while rays featuring both bottom and surface bounces experience losses of 90 dB to 140 dB with travel times varying from 36 s to 42 s.
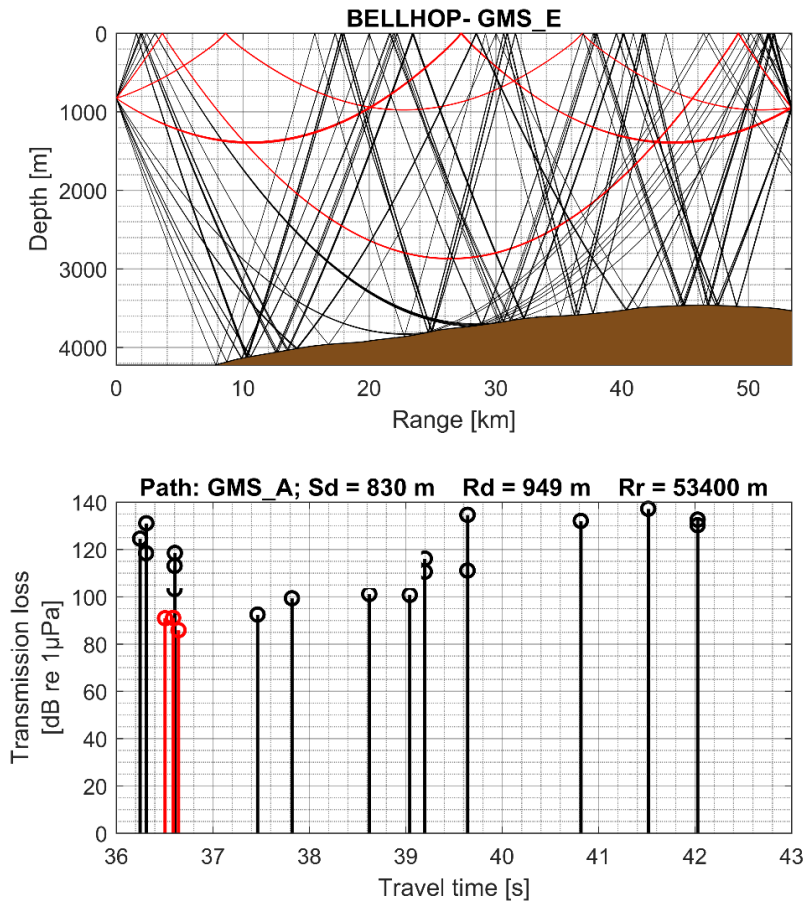
Figure 32: Exemplary raytracing plot of Eigenrays (top) and transmission loss over traveltime (bottom) for GMS. In both plots: Rays with surface bounces only in red, bottom bounces only in black. Source depth (Sd) is 830 m, recorder depth (Rd) is 949 m and range (Rr) is 53.4 km. No ice, surface with vacuum above.

To calculate travel time and transmission loss along GMT 2015 for oceanic conditions with sea ice present, two different *thin sea ice* conditions from 1 May (scenario s2) and the 1 June 2015 (scenario s3) are employed (Figure 33).
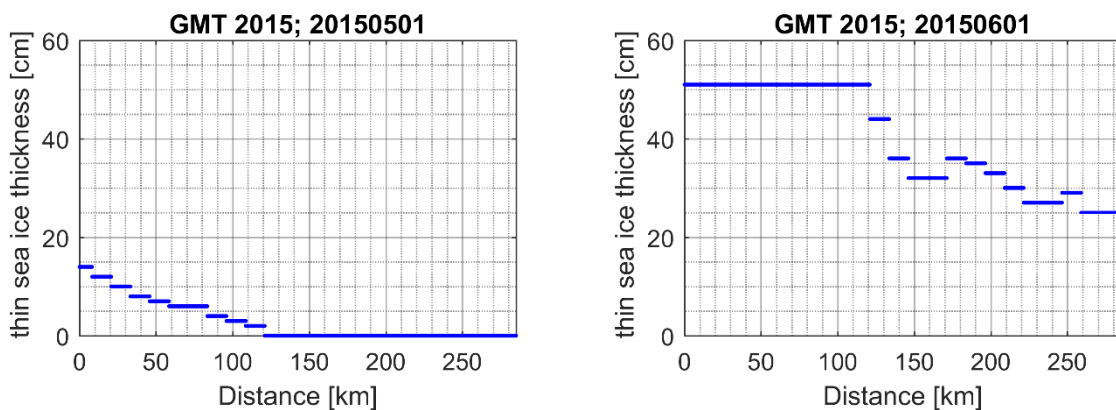
Figure 33: Thin sea ice thickness conditions that were used as model input, leading to the results in Figure 34 and Figure 36. Left: scenario s2: May 1 2015, right: scenario s3 June 1 2015.

The upper plot in Figure 34 shows the output for an ice-free scenario with vacuum capping the sea surface (scenario s1). The second and third stem plots represent the two ice-covered scenarios s2 and s3. Only minor differences are apparent between all three scenarios. Rays without bottom bounces exhibit no differences in time of arrival and transmission loss, while rays with bottom and surface bounces seem to be influenced slightly by the ice canopy as modelled here.
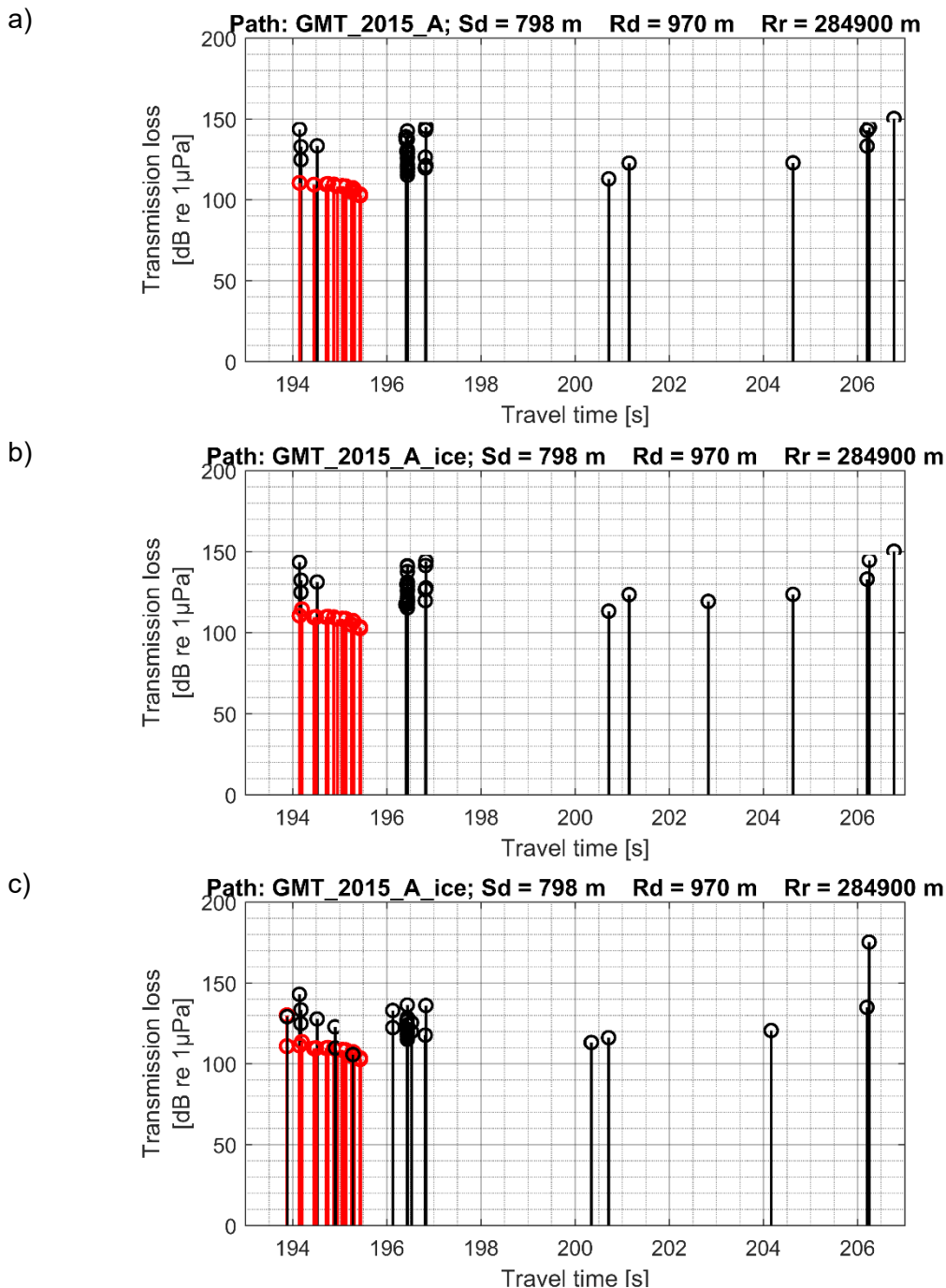
Figure 34: Stem plots represent the transmission loss in dB for Eigenrays at acoustic recorders of the analyzed path GMT 2015. Red are all Eigenrays which have surface contact only, while black stems represent Eigenrays with surface and bottom contact. X-axis represents the travel time of the Eigenrays in seconds. a) surface is modelled as smooth, ice-free boundary with vacuum above; b) ice cover from May 1 2015; c) ice-cover from June 1 2015 (see Figure 33).

The modelled coherent transmission loss exhibits significant variability with regard to the receivers location in the sound field (Figure 35, a)). Apart from the increase with distance to the sound source, transmission loss at the sound source depth displays a high variability (Figure 35, b)).

a)

b)
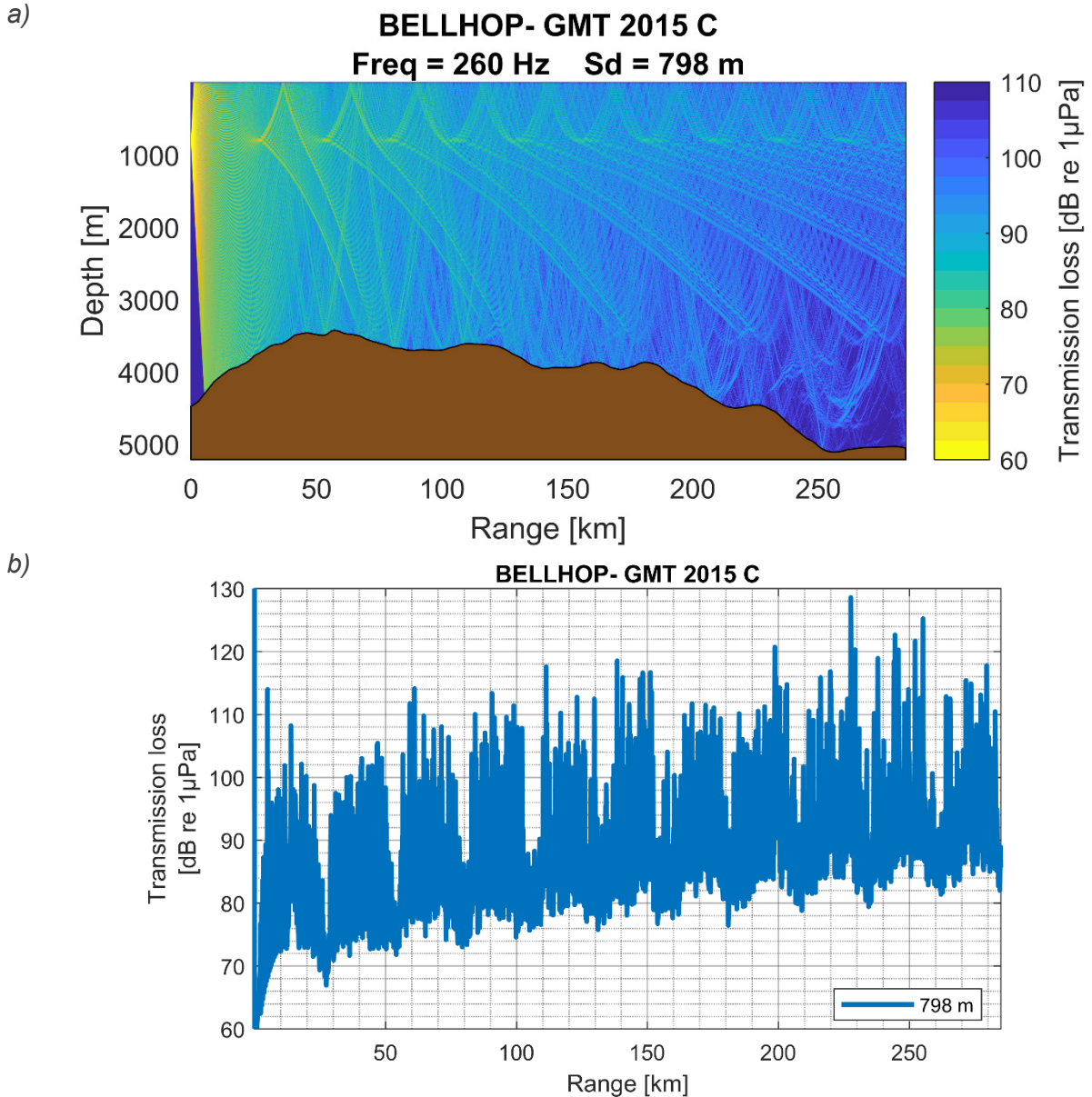
Figure 35: Coherent transmission loss for ice-free, vacuum above surface scenario (s1) on path GMT 2015. Horizontal resolution is 10m, vertical resolution is 1m. Sound field along path in a) and transmission loss in sound source depth at 798 m in b)

Figure 36 presents the modelled transmission loss in dB re 1µPa for path GMT 2015 with the three previously described ice scenarios. Plots in the first column present the TL at depths between 600 m and 1000 m for the last km of the transmission. Horizontal displacement of a receiver by a couple of 100 m yields differences of over 20 dB. A close up on the transmission loss at the assumed recorder distance and in depths from 700 m to 1200 m in the second column of Figure 36 reveals minor changes in the transmission loss between ice scenarios. Lowest transmission loss is located at depths some meters above the mooring depth of the

58

sound source. The result indicates a low variability for the transmission loss close to and slightly above the deployment depth of the sound source. However, variations within the displayed depth limits can exceed 30 dB.
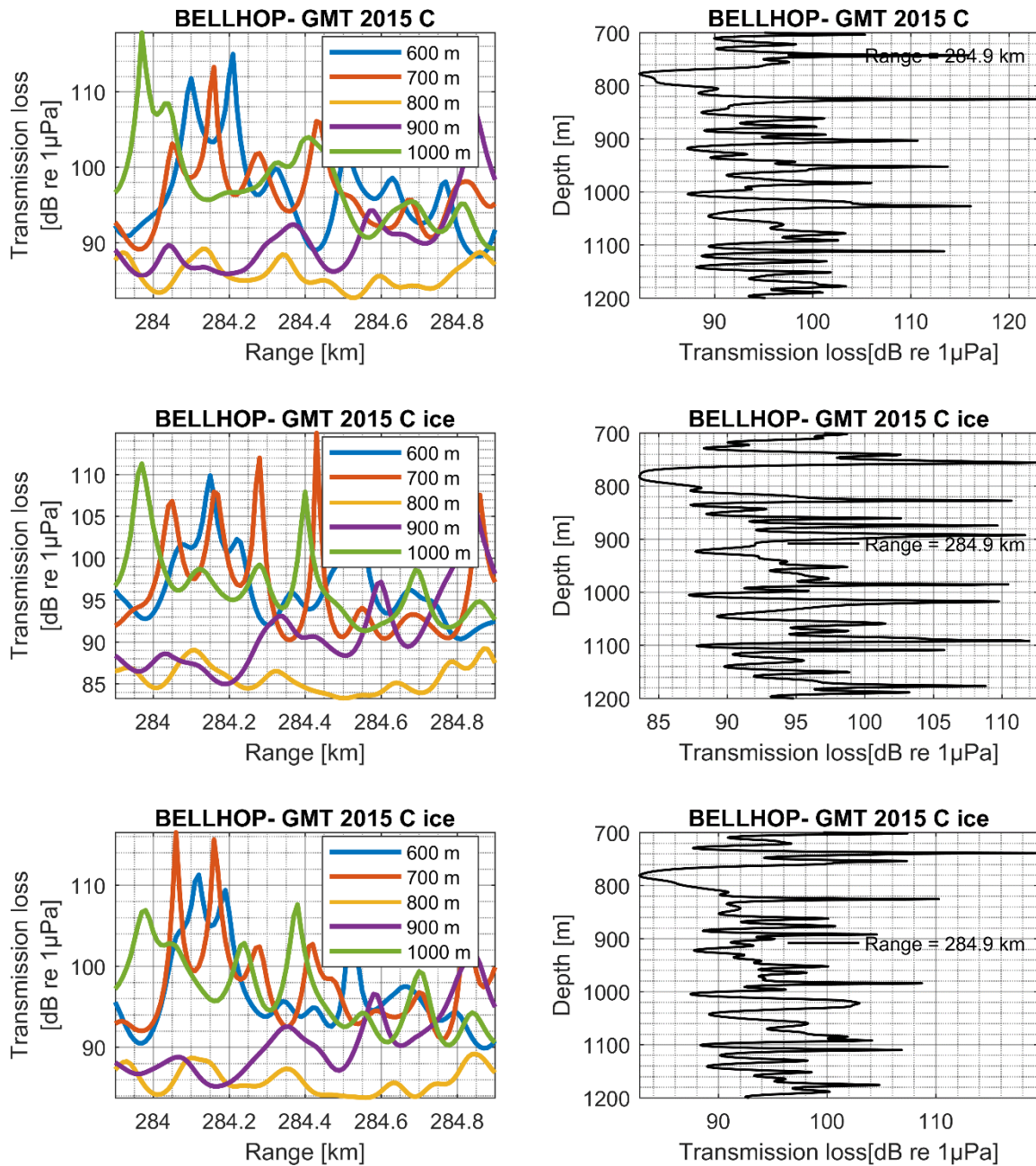
Figure 36: Transmission loss simulation for GMT 2015 with three different ice scenarios .First row: no ice with vacuum above. Second and third row: ice conditions a) and b) described in Figure 33.

5. DISCUSSION

The results from Chapter 4.4 demonstrate increased propagation losses of RAFOS signals in the presence of sea ice, with a maximum of about 10dB additional TL towards the end of the winter season for both the Weddell Sea and the Greenwich Meridian sections. Reception of RAFOS signals failed altogether for the Weddell Sea path after June, with no recovery of detections observable prior to the end of the recording in mid-October. In this case, one might suspect a complete failure of the Weddell Sea sound sources, for the period after June when recordings contained no RAFOS signals. However, passive acoustic recordings from recorders hosted by the same mooring as the respective source confirmed that both sound sources in AWI208 and AWI209 emitted signals through the entire period.

The increase of transmission loss on path GMT 2015 last from May until December. Transmission loss reaches additional 10dB relative to TL during ice-free periods. TL improves rapidly with the onset of the melting season (December) and has fully recovered in January. While paths GMN and GMT 2013 exhibited the same rate of increase, GMS, with 53 km the shortest of all analyzed paths, displayed rather constant TLs, though with high variability throughout the recordings. Unfortunately, data from GMT 2013 was only available until mid-July. Therefore, data from GMT paths in 2013 and 2015 could not be compared for the whole period. Nevertheless, at the time when recordings ended, GMT 2013 displayed an equal transmission loss (+7 ±1 dB) as GMT 2015 by the same time of year.

In the Weddell Sea, the eastward paths WSE1 and WSE2 show less change in TL between summer and winter (+10dB in winter) than observed in the westward direction (WSW, +16dB). (Table 6).

As sea ice concentration and thickness varies highly on temporal and spatial scales, differences in the distribution of different ice types along the propagation paths might appear to be a plausible cause for the observed differences between paths. Unfortunately, the available sea ice data does not provide information at the resolution to resolve these differences in detail. A modelling approach using ice statistics might be useful in this case.

Some recorded signals display only partial RAFOS signals with high SPL in the spectrograms (Chapter 4.4.2, Figure 14, Figure 15 and Figure 16). Even on subsequent days, signal quality appears to vary strongly. Multipathing could have an influence on the signal quality by destructive interference between parts of the signal.

Correlation coefficients of received RAFOS signals decreased with decreasing received level. Hence, correlation quality is generally declining when sea ice is present. While the growth of

sea ice also results in lower ambient noise levels, the ensuing partly improved SNR did not result in improved correlation cofficients.

The accuracy of time-of-arrival was not correlated with the waxing and waning of the sea ice concentration and *thin sea ice thickness*. Plausible ToAs extended for all paths examined at least 3 months into the winter season (estimated from the time of freezing onset), if not spanning across the entire winter. Data from the Weddell Sea paths, with a distance of 432 km the longest paths of this analysis, show the complete loss of plausible *relative ToA*s from the correlation three months after the beginning of sea ice formation (early April). After July, *ToA* is rather randomly distributed until the end of recordings in mid-Octobre. This delayed transition from valid to randomly scattered ToAs might be caused by change in sea ice topography after the initial *thin sea ice* formation. *Thin sea ice thickness* data reaches its upper limit of 50 cm in the Weddell Sea in May, suggesting greater ice thicknesses thereafter for this region. Deformation due to mechanical pressure and increasing snow coverage could further affect transmitted signals.

Including additional ice properties into the analysis, for instance data on ice thickness > 50 cm, snow coverage, floe sizes or under-ice roughness could help resolving the relation between the increase of transmission loss and ice type. Such data might not only pave the way for an explanation of the complete loss of signal for the Weddell Sea propagation paths, but also help explaining the difference in the evolution of transmission loss throughout the ice season between the Weddell Sea data and data from the Greenwich Meridian.

Having noted these empirical dependences between sea ice cover, ice cover age and TL, acoustic propagation modelling might hold on clue on the underlying physical mechanisms. The modelling results show that rays with bottom bounces generally result in higher TL and longer travel times than rays without any bottom bounce. Rays without bottom bounces are hence of higher relevance for the empirical signal detection than bottom bounced rays. Hence, rendering changes at the surface is most significant in determining the effective transmission loss. This notion is supported by the finding that, regardless of the ice situation, TL along GMS featuring only 1 or 2 surface bounces, is more or less constant.

While empirical evidence exists, that increased numbers of surface bounce at sea ice result in increased TL, acoustic propagation modelling fails to reproduce these findings. The inclusion of sea ice cover in the model runs resulted only in a limited effect on the transmission loss of single rays between the three ice scenarios chosen (up to 2 dB). This might result from sea ice type used in the model. Ice cover was modelled as a homogeneous, isotropic, elastic-plate using parameters from the literature and sea ice thicknesses of up to 50 cm only. Hence, the propagation modelling results can only be regarded as an indication on the impact of sea ice rather than a perfect match to the actual sea-ice conditions. Even though Yang and Votaw

(1981) regarded the impact of smooth, flat sea ice as the most significant influencing factor on transmission loss for frequencies between 200 Hz and 1 kHz, the inclusion of additional sea ice parameters, as mentioned for the statistical analysis above, could test this assumption. Modelling the sea ice canopy using the Monte Carlo model similar to Alexander et al. (2016) might provide a proxy for the currently unavailable details of the distribution of ice types during winter.

Nevertheless, even if such information on wintertime sea ice properties were available, any modelling including the roughness of the sea ice would require a reconsideration of the model type used. At a frequency of 260 Hz, the wavelength is 5.7 m, necessitating the resolution of the included surface structures to be higher than 5.7 m (i.e. shorter). Hence, the BELLHOP model would presumably not be capable of correctly including the sea ice roughness or ridging for frequencies around 260 Hz.

While the modelled influence of the ice coverage on transmission loss was small, it appears to be strongly influenced by the receiver's horizontal and vertical position relative to the sound source. Overall, lowest and most constant TL values within ±3 dB were modelled for receiver depths of up to 40 m shallower than deployment depth of the source (nominal deployment depth of 798 m) on path GMT 2015. On the longer path WSE1 in the Weddell Sea the depths of nearly constant TL within ±3 dB are located between 820 m and 880 m receiver depths, with the sound source position moored at a nominal instrument depth of 856 m.

To evaluate the impact of instrument depths on TL, depth data from the CTD recorders moored alongside sound sources and recorders were consulted. Instruments in moorings AWI208 and AWI209, i.e. the Weddell Sea paths, experienced little deviation from their deployment depth, whereas instruments in AWI229, part of paths GMN, GMT 2013 and GMT 2015 were suppressed by up to 160 m. Figure 11 in Chapter 4.2 illustrates this behavior. Adding floatation to moorings would stabilizing sound source depth and thus help limiting TL.

Validity of analysis

Table 6 summarizes transmission losses for the various approaches. The analytical calculation of transmission losses for ice-free conditions in Chapter 4.4.1 yielded values (Column Analytical/ice-free) within ±5dB of the values obtained by propagation modelling under ice-free conditions (Column Modelled/ice-free). By contrast, the mean empirical TL for ice-free months was up to 22 dB less than expected from the analytical results.

Path ID	Range r [km]	Mean water depth d [m]	Analytical Ice-free	Transmission Loss [dB] Empirical ice-free period	Transmission Loss [dB] Empirical ice covered period	Modelled minimum Ice-free; surface bounce only
WSW	432.5	4800	109	91±3	107±3	107
WSE1	432.5	4800	109	87±3	98±3	108
WSE2	432.5	4800	109	88±3	98±3	*
GMS	53.4	3819	82	83±3	82±3	80
GMN	226.8	4144	96	89±3	96±3	*
GMT 2013	280.1	4108	99	92±3	94±3	100
GMT 2015	284.9	4082	100	93±3	100±3	103

Table 6: Comparison of transmission loss from calculation in Chapter 4.4.1 , analysis of recordings in Chapter 4.4.3 and model results in Chapter 4.5.The following months were chosen to represent ice-free months: Weddell Sea: February to April; Greenwich Meridian: January to April; months with ice coverage were chosen as follows: Weddell Sea: May and June; Greenwich Meridian: June to November. The asterix (*) indicates configurations for which no calculations were performed. The uncertainty of the empirical evaluation contains measurement uncertainties for the sound source SPL and of the recorder calibration.

In this study, ToA was used as independent qualifier on whether the ToA and correlation coefficient produced by the correlation algorithm represented a valid RAFOS signal or rather random noise. This is possible due to the fact, that both source and receiver are moored and hence the expected ToA could be calculated and compared with the empirically determined ToA. Considering the validity of ToAs is necessary on the one hand to exclude invalid data from subsequent calculations and plots, but also to examine data – rather than noise – when trying to understand the conditions that shape RAFOS performance. For calculations of mean transmission loss, a threshold of 5 s was set for the maximum deviation of the empirical from the fitted ToA, i.e. relative ToA$_{rel}$. This constraint impacted minimally on mean TL estimated for the Greenwich Meridian while Weddell Sea data after June 2013 was affected strongly with almost no data point passing this threshold. Notably, the primary qualifier, correlation height, was shown not to provide a unique indication of a detection's validity: correct ToAs have been obtained in conjunction with even relatively low correlation heights.

As correlation heights are not comparable to each other because of the means of normalization in this thesis, using another metric for normalization might improve the comparability between the analyzed paths.

Porter describes the calculation of the propagating rays as Gaussian Beams the most accurate option as implemented in BELLHOP, a notion this study follows by selecting the corresponding setting for the model runs conducted here. The accuracy of the interference pattern of the BELLHOP model is considered by Porter (2011) to be in excellent agreement with KRAKEN and SCOOTER results. He compares the interference pattern of the results from an example with 50 Hz signals for different settings. As a result he finds that the fine details of the interference pattern are reproduced correctly. On the downside of the comparison he identifies some artifacts typical for the ray theory, like perfect shadows and caustics for some of the beam settings. For better accuracy, they therefore invoke the Gaussian beam option. As a result this produces some leakage energy in the shadow zones and smooths out the caustics (Porter and Bucker 1987). Nevertheless, some of the strong variations in the sound field modelled with the BELLHOP algorithm might be related to these disadvantages of ray theory towards other model types.

RAFOS array performance

In the Antarctic summer RAFOS signals were detected by the used correlator in this analysis over distances as much as 430 km. Nevertheless, in winter, when tracking of the floats beneath the surface by detection of the RAFOS signals is most needed, the signal appears to fail for distances somewhere between 280 km and 430 km. As discussed previously, according to the model results, the vertical but also small-scale horizontal position in the water column seems to play a significant role in the performance of the signal detection. Therefore, direct comparison between the data from the passive acoustic recorders, moored at 1000 m depth, and the Argo floats, drifting at 800 m depth, is questionable. Nevertheless, vertical positions close to the mooring depth of the source were found to hold the best probability for signal detection. Vertical repositioning of the sound source might improve the propagation by lowering the number of surface bounces along the path. A modelling approach to test several deployment depths for the sound sources could be useful. Nevertheless, the drifting depth of the floats would probably need to be adjusted in this case. In consequence of the results from depth data for instruments in mooring AWI229, where instruments drop by up to 160 m, a new mooring layout could be a first improvement for the array.

Impact on other areas of research

The significant decrease in transmission loss during austral winter also affects other fields of studies. The acoustic recorders were initially deployed for the investigation of distribution and migration patterns of various marine mammal species. With the gained knowledge on changes in the propagation of the RAFOS signal during austral winter, results from the studies on marine mammals need to be carefully evaluated. The Comparison of winter data with summer data might be biased.

6. CONCLUSION

On all paths, decreasing correlation height correlates clearly with the decrease of measured sound pressure levels of the RAFOS signal. Building sea ice cover also leads to lower noise levels in the frequency band of interest. A significant correlation between the resulting SNR and correlation heights is missing. Analysis of recorded RAFOS signals implies an influence of sea ice coverage on the signal transmission loss. Due to the lack of data regarding the ice type and properties, it could not be determined if this was related to greater changes in the ice thickness, mechanical feature or changing properties of the ice canopy.

Modelling results suggest strong variations of transmission loss, depending on the horizontal and vertical position of the sound source/receiver pairing. Modelled rays with surface bounce only have shorter travel times and lower transmission loss. This is true for the ice-free scenario, as well as both scenarios with ice-coverage. An impact of the sea-ice on the modelling results is present, however small.

Additional sea ice data included in future analysis could improve the analysis as well as the modelling approach and reveal an additional impact of different ice types on the quality of the propagating RAFOS signal.

ACKNOWLEDGEMENTS

I would like to thank my colleagues in the Physical Oceanography section at the AWI for their support during my 'Master's experience'. Thank you Matthes, Rainer, Gerd, Ilse, Karolin, Elke and Michael for your encouragement, friendship and coffee. I am happy to have the possibility to work with such great people.

I am very grateful to Olaf Boebel and Torsten Kanzow for accepting and supporting my efforts to finish this thesis and for being great superiors. Thank you Olaf for your efforts to improve my scientific writing skills and for the knowledge on the subject you shared with me, I hope most of it will stick.

I will always be grateful to the late Eberhard Fahrbach who made this possible in the first place.

Many thanks to Prof. Kraus at the Hochschule Bremen, for his feedback and patience while I was writing this thesis.

Moreover, I would like to thank my beloved family: this would not have been possible without my husband Ulli who supported me through this course with immense patience and, in parallel, through two pregnancies and the birth of two children. Big hugs to our son Florian who accepted me sitting at the desk working instead of playing with him. Last but not the least, many thanks to my parents taking their time and looking after our two children in times of need.

I. LIST OF FIGURES

II. LIST OF TABLES

III. LITERATURE

Alexander, P., A. Duncan, N. Bose, and D. Smith. 2013. MODELLING ACOUSTIC TRANSMISSION LOSS DUE TO SEA ICE COVER. Acoustics Australia **41**.

Alexander, P., A. Duncan, N. Bose, and G. Williams. 2016. Modelling acoustic propagation beneath Antarctic sea ice using measured environmental parameters. Deep Sea Research Part II: Topical Studies in Oceanography **131**:84-95.

Bennett, T. 2009. Centre for Marine Science and Technology-Underwater Acoustic Propagation Modelling software-AcTUP V2. 2L.

Boebel, O. 2013. The expedition of the research vessel "Polarstern" to the Antarctic in 2012/2013 (ANT-XXIX/2). Alfred Wegener Institute for Polar and Marine Research, Bremerhaven.

Breitzke, M., and T. Bohlen. 2010. Modelling sound propagation in the Southern Ocean to estimate the acoustic impact of seismic research surveys on marine mammals. Geophysical Journal International **181**:818-846.

Etter, P. 2003. Underwater Acoustic Modeling and Simulation. Spon Press, New York.

Fretwell, P., H. D. Pritchard, D. G. Vaughan, J. L. Bamber, N. E. Barrand, R. Bell, C. Bianchi, R. G. Bingham, D. D. Blankenship, G. Casassa, G. Catania, D. Callens, H. Conway, A. J. Cook, H. F. J. Corr, D. Damaske, V. Damm, F. Ferraccioli, R. Forsberg, S. Fujita, Y. Gim, P. Gogineni, J. A. Griggs, R. C. A. Hindmarsh, P. Holmlund, J. W. Holt, R. W. Jacobel, A. Jenkins, W. Jokat, T. Jordan, E. C. King, J. Kohler, W. Krabill, M. Riger-Kusk, K. A. Langley, G. Leitchenkov, C. Leuschen, B. P. Luyendyk, K. Matsuoka, J. Mouginot, F. O. Nitsche, Y. Nogi, O. A. Nost, S. V. Popov, E. Rignot, D. M. Rippin, A. Rivera, J. Roberts, N. Ross, M. J. Siegert, A. M. Smith, D. Steinhage, M. Studinger, B. Sun, B. K. Tinto, B. C. Welch, D. Wilson, D. A. Young, C. Xiangbin, and A. Zirizzotti. 2013. Bedmap2: improved ice bed, surface and thickness datasets for Antarctica. The Cryosphere **7**:375-393.

Greene, C. A., D. E. Gwyther, and D. D. Blankenship. 2017. Antarctic Mapping Tools for Matlab. Computers & Geosciences **104**:151-157.

Grosfeld, K., R. Treffeisen, J. Asseng, A. Bartsch, B. Bräuer, B. Fritzsch, R. Gerdes, S. Hendricks, W. Hiller, G. Heygster, T. Krumpen, P. Lemke, C. Melsheimer, M. Nicolaus, R. Ricker, and M. Weigelt. 2016. Online sea-ice knowledge and data platform <www.meereisportal.de>. Pages 143-155. Alfred Wegener Institute for Polar and Marine Research & German Society of Polar Research, Bremerhaven.

Huntemann, M., G. Heygster, L. Kaleschke, T. Krumpen, M. Mäkynen, and M. Drusch. 2014. Empirical sea ice thickness retrieval during the freeze-up period from SMOS high incident angle observations. The Cryosphere **8**:439-451.

ISO, T. 2017. ISO 18405:2017(E) - Underwater acoustics — Terminology. International Organization for Standardization.

Jensen, F. B., W. A. Kuperman, M. B. Porter, and H. Schmidt. 2011. Computational Ocean Acoustics. Springer Publishing Company, Incorporated.

Jezek, K. C., T. K. Stanton, A. J. Gow, and M. A. Lange. 1990. Influence of environmental conditions on acoustical properties of sea ice. The Journal of the Acoustical Society of America **88**:1903-1912.

Klatt, O., O. Boebel, and E. Fahrbach. 2007. A Profiling Float's Sense of Ice. Journal of Atmospheric and Oceanic Technology **24**:1301-1308.

König, H., and W. Zenk. 1992. Principles of RAFOS technology at the Institut für Meereskunde Kiel.

Kuhn, G., and M. E. Weber. 1993. Acoustical characterization of sediments by Parasound and 3.5 kHz systems: Related sedimentary processes on the southeastern Weddell Sea continental slope, Antarctica. Marine Geology **113**:201-217.

Lurton, X. 2002. An introduction to underwater acoustics: principles and applications. Springer Science & Business Media.

Marchenko, A., and A. Makshtas. 2005. A dynamic model of ice ridge buildup. Cold Regions Science and Technology **41**:175-188.

Medwin, H., and C. S. Clay. 1997. Fundamentals of acoustical oceanography. Academic Press.

Melles, M., and G. Kuhn. 1993. Sub-bottom profiling and sedimentological studies in the southern Weddell Sea, Antarctica: evidence for large-scale erosional/depositional processes. Deep Sea Research Part I: Oceanographic Research Papers **40**:739-760.

Menze, S., D. P. Zitterbart, I. van Opzeeland, and O. Boebel. 2017. The influence of sea ice, wind speed and marine mammals on Southern Ocean ambient sound. Royal Society Open Science **4**.

Michels, K. H., G. Kuhn, C.-D. Hillenbrand, B. Diekmann, D. K. FÜtterer, H. Grobe, and G. Uenzelmann-Neben. 2002. The southern Weddell Sea: combined contourite-turbidite sedimentation at the southeastern margin of the Weddell Gyre. Geological Society, London, Memoirs **22**:305-323.

Porter, M. B. 2011. The bellhop manual and user's guide: Preliminary draft. Heat, Light, and Sound Research, Inc., La Jolla, CA, USA, Tech. Rep.

Porter, M. B., and H. P. Bucker. 1987. Gaussian beam tracing for computing ocean acoustic fields. The Journal of the Acoustical Society of America **82**:1349-1359.

Rodriguez, O. C. 2008. General description of the BELLHOP ray tracing program. Physics Department Signal Processing Laboratory Faculty of Sciences and the University of the Algarve Tecnologia (Galician), Version **1**.

Rossby, T., D. Dorson, and J. Fontaine. 1986. The RAFOS System. Journal of Atmospheric and Oceanic Technology **3**:672-679.

Spreen, G., L. Kaleschke, and G. Heygster. 2008. Sea ice remote sensing using AMSR-E 89-GHz channels. Journal of Geophysical Research: Oceans **113**.

Stommel, H. 1955. Direct measurements of sub-surface currents. Deep Sea Research (1953) **2**:284-285.

Swallow, J. C. 1955. A neutral-buoyancy float for measuring deep currents. Deep Sea Research (1953) **3**:74-81.

Thorp, W. H. 1967. Analytic description of the low-frequency attenuation coefficient. The Journal of the Acoustical Society of America **42**:270-270.

Wooding, C. M., H. H. Furey, and M. A. Pachece. 2005. RAFOS float processing at the Woods Hole Oceanographic Institution. WOODS HOLE OCEANOGRAPHIC INSTITUTION MA.

Yang, T. C., and C. W. Votaw. 1981. Under ice reflectivities at frequencies below 1 kHz. The Journal of the Acoustical Society of America **70**:841-851.

Yew, C. H., and X. Weng. 1987. A study of reflection and refraction of waves at the interface of water and porous sea ice. The Journal of the Acoustical Society of America **82**:342-353.